



Is the CO₂ methanation on highly loaded Ni-Al₂O₃ catalysts really structure-sensitive?



Dennis Beierlein^{a,*}, Dorothea Häussermann^a, Mirko Pfeifer^b, Thomas Schwarz^b, Klaus Stöwe^b, Yvonne Traa^{a,*}, Elias Klemm^a

^a Institute of Chemical Technology, University of Stuttgart, 70550 Stuttgart, Germany

^b Institute of Chemistry, Chemnitz University of Technology, 09111 Chemnitz, Germany

ARTICLE INFO

Keywords:

Power to gas
CO₂ methanation
Highly loaded Ni catalysts
Structure-activity relationship
Structure insensitivity

ABSTRACT

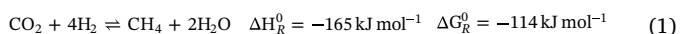
Highly loaded Ni-Al₂O₃ catalysts (14–88 wt.-% Ni) were prepared by dry impregnation, wet impregnation, deposition precipitation and coprecipitation and tested in the CO₂ methanation. By means of ICP-OES, XRD, TPR, H₂ chemisorption, N₂ physisorption and thermogravimetry, different Ni species were identified, and their dependence on the synthesis method and the Ni loading was investigated. The catalysts prepared had Ni particle sizes of 5–91 nm and Ni surface areas of 5–51 m² g⁻¹. It could be shown that the turnover frequency (TOF) does not depend on metal-support interactions, the metal-support interface or the particle size. Hence, the CO₂ methanation on Ni-Al₂O₃ catalysts is clearly a structure-insensitive reaction. There is a linear correlation between the conversion and the Ni surface area at constant modified residence time. Hence, catalysts with the highest Ni surfaces, i.e., the samples prepared by deposition precipitation and coprecipitation, reached the highest weight time yields. The prerequisites for high Ni surface areas at high Ni loadings could be elucidated: During the synthesis, Ni has to be able to completely penetrate the mesopores of the support. Furthermore, a linear correlation between the selectivity to CO and the weight percentage of the impurity Na could be revealed. The stability of the supported catalysts was highly dependent on the spatial distribution of Ni and the stability of the support: A high dispersion or the presence of unsupported Ni reduced the stability. Furthermore, the stability of the supported catalysts was smaller than the one of the coprecipitated catalysts, where the stability decreased with increasing $n_{\text{Ni}}/n_{\text{Al}}$.

1. Introduction

In an effort to reduce the CO₂ emission and the consumption of fossil feedstock, renewable energy is gaining importance. The disadvantage of renewable energy is that it is highly dependent on the weather, the daytime and the season. Hence, energy storage is necessary for a constant power supply. The „Power to Gas“ (PtG) process is a promising concept for energy storage, where surplus electricity is used for the production of H₂ via H₂O electrolysis. Afterwards, the H₂ can be converted with CO₂ from coal-fired power plants, the cement industry, biogas plants or the atmosphere to CH₄. The thus produced „substitute natural gas“ (SNG) can be used for chemical energy storage and afterwards again for power generation, as fuel in the mobility sector or in industry and the private sector. Several reviews are devoted to the PtG process [1–3], which also give an overview over existing pilot and demonstration plants [4,5].

The catalytic CO₂ methanation was first described by Sabatier and

Senderens [6]. Due to the kinetic limitation, a catalyst is needed for significant reaction rates [7]. Thermodynamically, the methanation is favored and clearly exothermic (Eq. (1)):



Up to now, a plethora of catalysts with different metals (Ni, Co, Fe, Cu, Ru, Rh, Ir, Pd, Pt [8–12]) and supports (TiO₂, SiO₂, SiO₂-Al₂O₃, α -Al₂O₃, γ -Al₂O₃, MgAl₂O₄, MgO, ZrO₂, CeO₂, C, MSN, MCM-41, SBA-15, HY, USY [13–19]) have been investigated. Between 1973 and 2018, different reviews appeared on the catalyst [20–26] and the reaction mechanism [27] of the CO₂ methanation. With regard to the supports, it has been shown that aluminum oxides are good supports [13–15]. In addition, Al₂O₃ supports are cheap and in large amounts commercially available. Ni, Ru and Rh are the best active metals for the CO₂ methanation with Ni being favored due to the low price.

For an industrial application, catalysts with high selectivity, space time yield (STY) and stability are favored. The first step of a tailoring of

* Corresponding authors.

E-mail addresses: dennis.beierlein@itc.uni-stuttgart.de (D. Beierlein), yvonne.traa@itc.uni-stuttgart.de (Y. Traa).

the catalyst is to find a correlation between the microscopic properties of the catalyst and the activity in the CO₂ methanation. The literature on this aspect is not conclusive. Some authors assume that the activity depends on the nickel particle size and that the particle geometry has a significant influence (structure-sensitive reaction) [28–31]. Koschany et al. [32] observe that the weight time yield of coprecipitated Ni-AlO_x catalysts increases linearly with the metal surface, whereas other properties such as the BET surface area and the particle size do not have a significant influence (structure-insensitive reaction). However, an influence of the support and the particle size is not completely ruled out.

Structure-activity relationships determine which catalyst properties have to be modified in order to increase the STY. In the case of a structure-sensitive reaction, the amount of small metal particles should be maximized. For structure-insensitive reactions, only the metal surface of the catalyst is decisive. If the structure-activity relationships are clear, the question is how the catalyst properties can be correspondingly modified during their preparation, which is then the second step of the catalyst tailoring. There is ample literature available for the synthesis of Ni-Al₂O₃ catalysts demonstrating that the catalyst properties depend on the synthesis method [33–37], the Al₂O₃ polymorph [38,39], the Ni precursor [40–42], the metal loading [43–45] and the thermal treatment (calcination/reduction) [43,46].

Generally, it is observed that increasing the metal loading for supported catalysts leads to larger metal particles, decreasing metal dispersion, and exerts a negative influence on the texture of the support [44,45,47–49]. Therefore, only a few studies were devoted to the synthesis of supported catalysts with high metal loadings which confirm that an increasing metal loading leads to larger particles and a smaller dispersion [50–52]. However, sometimes it is observed that the metal surface increases with increasing metal loading. Hence, the increasing metal loading can compensate for the decrease in dispersion by increasing the Ni surface. Hu et al. [53] point out that supported Ni catalysts with Ni loadings ≥ 50 wt.-% are industrially used for hydrogenation [21,54], even though there are only a few studies with Ni loadings larger than 20 wt.-%.

In the literature, Ni catalysts with Ni loadings ≥ 50 wt.-% are almost always synthesized via coprecipitation [55–61]. During coprecipitation and sol-gel synthesis, the Ni particles form from mixed oxides, whereas in supported catalysts, the Ni particles form from NiO and different Ni surface species (Ni(Al)O_x: Al³⁺ ions dissolved in NiO, Al(Ni)O_x: Ni²⁺ ions dissolved in γ -Al₂O₃). Thus, due to the different Ni species, the catalytic properties, the metal-support interactions, the extent of reduction and the catalyst stability of supported catalysts with high Ni loading can be considerably different from the ones of coprecipitated catalysts.

Hence, this short survey on the literature shows that it has not been elucidated yet which catalyst properties determine the activity in the CO₂ methanation and that there are only a few studies on the influence of the preparation method and highly loaded Ni catalysts. Koschany et al. [32] stress that for structure-activity relationships investigations on catalysts which were not prepared by coprecipitation are necessary. In addition, comprehensive and systematic studies are needed to identify those parameters of the preparation method which control the Ni surface and the Ni particle size of highly loaded Ni catalysts.

Therefore, the aim of this work is to determine the structure-activity relationships of the CO₂ methanation. If we can elucidate the influence on the activity on the microscopic level, the catalyst properties can be tailored. This requires a detailed understanding of the preparation method. Hence, we prepared catalysts with Ni mass fractions between 14 and 88% with four different methods, i.e., dry impregnation (DI samples; this method is also called incipient wetness impregnation), wet impregnation (WI samples), deposition precipitation (DP samples) and coprecipitation (CP samples), and tried to understand the fundamental relationship between preparation method, Ni mass fraction, particle size/dispersion and catalyst stability. Thus, we gained new

insight into the structure-activity relationships of the CO₂ methanation, which is an important step towards a knowledge-based development of catalysts for the industrial CO₂ methanation.

2. Experimental section

2.1. Catalyst preparation

The catalysts were named after the Ni content and the preparation method: xY, x = Ni mass fraction of the reduced and passivated catalyst, Y: abbreviation of the preparation method (WI: wet impregnation, DI: dry impregnation, DP: deposition precipitation, CP: coprecipitation).

During *wet impregnation*, the γ -Al₂O₃ support was provided in a Teflon vessel, and the Ni salt solution with a volume significantly higher than the pore volume of the support was added. The metal salt solutions contained, according to the desired Ni loading, different masses of Ni(NO₃)₂·6H₂O (Table S2). On a flat orbital shaker (IKA, model: KS 260 basic), the water was vaporized at 60 °C. Afterwards, the samples were dried for 12 h at 150 °C and calcined for 3 h at 400 °C (heating rate for drying and calcination: 1 °C min⁻¹). According to this procedure, the samples 30WI to 72WI were prepared. For samples with higher Ni loadings, the impregnation was carried out in two steps, and the samples were dried and calcined between the two impregnation steps and afterwards again (81WI and 88WI).

During *dry impregnation*, defined Ni(NO₃)₂·6H₂O solutions were added with an Eppendorf pipette to the dry γ -Al₂O₃ support (Table S3) and mixed with a speed mixer (Hauschild Engineering, model: DAC 150 SP). Several impregnation steps Z were needed (Z = 2–7, Table S3). After each impregnation step, the samples were dried at 60 °C overnight and afterwards dried as described above. The calcination occurred only after the last impregnation step.

During *deposition precipitation*, the γ -Al₂O₃ support was suspended in 540 mL demin. water, and a solution of the corresponding amount of the Ni salt in a 1 M HNO₃ solution was slowly added (pH \leq 1, Table S4). Afterwards, a 5 M NaOH solution (pH \geq 14) was added with a micrometering pump (500 μ L min⁻¹), until a pH value of 10 was reached. The suspension was stirred for 1 h, left without stirring for 18 h, filtered and washed with 300 mL demin. water. To investigate the influence of higher Na contents, the 20DP sample was washed with only 200 mL demin. water. Then all samples were dried and calcined as described above.

The *coprecipitation* occurred after a modified method of He et al. [62]: In a three-necked flask, 50 mL of the corresponding 1 M metal salt solution (Table S5) were added with a droplet rate of 4–6 g min⁻¹ under stirring at 65 °C to 50 mL of a 0.8 M Na₂CO₃/1.2 M NaOH solution. Afterwards, the pH value was adjusted to 10 with a 3 M NaOH solution, and stirring was continued for 18 h. The product was filtered, washed three times with 30 mL demin. water, and dried at 80 °C for 8 h (heating rate: 2 °C min⁻¹).

The catalysts were pressed and sieved into particles of 0.200–0.315 mm size. The WI, DI and DP samples were pre-reduced externally in a quartz glass reactor. 0.5 cm quartz wool and 1.7 g catalyst were placed on the quartz glass frit of the reactor. The thermocouple was placed directly within the packed bed. The reduction occurred within 60 min at 600 °C (heating rate: 3 °C min⁻¹) with a volumetric flow of 400 mL min⁻¹ (30 vol.-% H₂ in N₂). For the reduction of the CP samples, conditions after He et al. [62] were applied, and the dried precipitates were reduced in flowing hydrogen (80–85 mL min⁻¹) at 500 °C within 60 min. Afterwards, all samples were cooled to ambient temperature (< 30 °C) and purged with 400 mL min⁻¹ nitrogen. For passivation, synthetic air was added to adjust the oxygen content to 0.1 vol.-%, resulting in a small heat evolution (< 45 °C). Once the samples had cooled down to ambient temperature, the oxygen content was within 5 min slowly increased to 1 vol.-%, and the catalysts were passivated overnight (1 vol.-% O₂ in N₂ with 60 mL min⁻¹).

2.2. Catalyst characterization

The Ni and Na mass fractions, w_{Ni} and w_{Na} , were determined by *optical emission spectroscopy* with inductively coupled plasma as excitation source (Varian; Vista-MPX CCD 17 Simultaneous ICP-OES). Values are related to the dry mass of the reduced and passivated catalysts. For N_2 *physisorption* measurements (Quantachrome; Autosorb IIIb), 0.1–0.3 g catalyst were degassed at 350 °C in vacuum ($p < 1 \text{ Pa}$) for 16 h, and afterwards, the adsorption and desorption isotherms were determined at –196 °C. The specific surface of the catalysts was measured at $p/p_0 = 0.05\text{--}0.3$ (BET method), and the pore volume at $p/p_0 = 0.96$. For an understanding of the textural changes of the support, the measured BET surface areas $S(\text{BET})$ and the measured pore volumes V_p were related to the support mass fraction with Eqs. (2) and (3) and then called modified BET surface area $S(\text{BET})_{\text{mod}}$ and modified pore volume V_p, mod . The pore size distributions for the adsorption and the desorption branch were calculated using the BJH method.

$$S(\text{BET})_{\text{mod}} = \frac{S(\text{BET})}{1 - w_{\text{Ni}}} \quad (2)$$

$$V_p, \text{mod} = \frac{V_p}{1 - w_{\text{Ni}}} \quad (3)$$

In a *powder X-ray diffractometer* (Bruker AXS, D8 Advance), diffractograms were recorded using monochromatic CuK_α radiation (40 kV, 30 mA). Angles 2θ between 5 and 80° were measured with a step length of 0.165° and a step time of 5 s. The different phases were identified using the Joint Committee on Powder Diffraction Standards (JCPDS). For the determination of the Ni and the NiO crystallite sizes, the full width at half maximum of the $\text{Ni}(200)$ and $\text{NiO}(220)$ reflections was determined and corrected with the Warren Eq. (4) using LaB_6 as reference.

$$\beta = \sqrt{\beta_{\text{observed}}^2 - \beta_{\text{reference}}^2} \quad (4)$$

The mean crystallite sizes d_c were calculated with the Scherrer Eq. (5) with the wavelength λ of the CuK_α radiation ($\lambda(K_{\alpha 1}) = 0.15406 \text{ nm}$), the Bragg angle θ at the peak of the respective reflection and the shape factor K_F with a value of 0.9 [63].

$$d_c = \frac{K_F \cdot \lambda}{\beta \cdot \cos\theta} \quad (5)$$

Temperature-programmed reduction (TPR) was performed using an automated gas sorption analyzer (Quantachrome; Autosorb-iQ). In order to avoid influences of the reaction conditions on the shape and position of the reduction peaks, appropriate conditions were chosen using criteria equations. For the empirical criteria of Monti and Baiker [64] $K = n_0 / \dot{V}_{\text{total}} c_0$ and Malet and Caballero [65] $P = \beta_{\text{H}} K$, values of $K = 120 \text{ s}$ and $P = 16 \text{ K}$ were set, where n_0 is the molar amount of the reducible species, \dot{V}_{total} the total volumetric flow, c_0 the H_2 concentration and β_{H} the heating rate. The weighed calcined catalyst mass was chosen in a way so that each measurement was performed with a constant NiO mass of 20 mg ($n_0 = 2.7 \cdot 10^{-4} \text{ mol}$). For the CP samples, the dried precipitation products were used, and a catalyst mass corresponding to $2.7 \cdot 10^{-4} \text{ mol Ni}^{2+}$ ions was weighed in. Prior to the measurement, the samples were pretreated in a helium flow (30 mL min^{-1}) for 15 min at 120 °C (heating rate: 20 °C min^{-1}) and afterwards cooled down to 50 °C. In a flow of 30 mL min^{-1} of 10 vol.-% H_2 in N_2 , temperatures from 50 to 950 °C were measured with a heating rate of 8 °C min^{-1} ($\beta_{\text{H}} = 0.13 \text{ K s}^{-1}$, $\dot{V}_{\text{total}} = 0.5 \text{ mL s}^{-1}$, $c_0 = 4.5 \cdot 10^{-6} \text{ mol mL}^{-1}$).

The extent of reduction f was determined (with a deviation of $\pm 4\%$) by *thermogravimetry* (Netzsch, STA 449F5 Jupiter). A catalyst mass of 20–40 mg was pretreated in argon for 90 min at 150 °C (heating rate: 2 °C min^{-1}). Afterwards, the samples were reduced for 60 min at 400 °C in 5 vol.-% H_2 in N_2 (heating rate: 5 °C min^{-1}), and then cooled down to 50 °C in N_2 . Subsequently, the samples were oxidized in synthetic air for 60 min at 400 °C (heating rate: 5 °C min^{-1}) and again

cooled down to 50 °C in N_2 . The WI samples were oxidized for 360 min at 430 °C. With the mass difference Δm measured at 50 °C before and after the oxidation, the extent of reduction was calculated with Eq. (6) with the Ni mass of the sample m_{Ni} and the mass of oxygen m_{O} for a complete reduction of Ni.

$$f = \frac{\Delta m}{m_{\text{Ni}} \left(\frac{m_{\text{O}}}{m_{\text{Ni}}} \right)} \cdot 100 = \frac{\Delta m}{m_{\text{O}}} \cdot 100 \quad (6)$$

The Ni surface area of the catalysts ($S(\text{Ni})$, in $\text{m}^2 \text{ g}^{-1}$), the dispersion D and the mean particle size (d_p , in nm) were calculated by static H_2 *chemisorption* measurements (Quantachrome, AUTOSORB-1C). For this purpose, the passivated catalysts were reduced in a hydrogen flow for 60 min at 400 °C, and the adsorption isotherm was determined at 40 °C. The Ni surface area was obtained by extrapolation of the linear range of the adsorption isotherm of the reversibly and irreversibly adsorbed H_2 to a pressure of 0 (V_{H_2} in mol g^{-1} related to the mass of the pre-reduced and passivated catalyst) assuming an adsorption stoichiometry of $\text{Ni:H} = 1$ and 6.49 \AA^2 per Ni atom. For the calculation of the dispersion, the extent of reduction f was taken into account according to Eq. (7) [66,67]:

$$D = \frac{1.17 \cdot 10^6 \cdot \frac{\text{g}}{\text{mol}} \cdot V_{\text{H}_2}}{w_{\text{Ni}} \cdot f} \quad (7)$$

The mean particle (which can consist of several crystallites) size $d_p(\text{Ni})$ was calculated after Bartholomew and coworkers [66,67] with Eq. (8):

$$d_p(\text{Ni}) / \text{nm} = \frac{97.1}{D} \quad (8)$$

2.3. Experimental setup

The catalytic experiments were carried out in an automated experimental rig. The reactant gas mixture was set with mass flow controllers (MFCs) from Bronkhorst. The pressure was regulated with a back pressure regulator from Bronkhorst. The reactor was a 316 L stainless steel tube with a diameter of 5 mm heated by an aluminum block. Isothermal conditions were ensured by using the heating system described in detail in [68]. The temperature of the fixed bed was measured in the first quarter of the fixed bed with a movable thermocouple of type K. All tubings after the reactor and the tubing directly in front of the reactor were heated to 230 °C in order to avoid condensation of the water formed in the reaction and to preheat the reactant gas.

During the catalytic measurements, the catalyst mass was chosen in a way that the Ni surface area was constant and equal to 2.5 m^2 . For ensuring an isothermal fixed bed, all samples were diluted with 2.8 g SiC with a particle size of 0.200–0.315 mm. The SiC particles were mixed with the passivated catalyst in a snap cap vial by carefully rotating the vial for 1 min. The glass frit of the reactor was covered with glass wool (about 5 mm height). The mixture of the catalyst and SiC was filled into the reactor using a paper funnel in order to avoid the buildup of electrostatic charges. The length of the fixed bed L changed between 8 and 11 cm depending on the catalyst mass and density. Prior to the measurement, the catalyst was reduced 1 h at 100 kPa and 400 °C in 30 vol.-% H_2 in N_2 . After cooling, the measurement started with a reactant mix of $\text{H}_2/\text{CO}_2/\text{Ar}$ in the ratio of 76/19/5 ($n_{\text{H}_2}/n_{\text{CO}_2} = 4$) and a pressure of 200 kPa. The volumetric flow was set so that the conversion was 30% at 300 °C. The turnover frequency TOF was determined within 6 h at 300 °C. After a bypass measurement at ambient temperature, the modified residence time was set to a constant value ($\tau_{\text{mod}} = \text{catalyst mass} / \text{total volumetric flow (STP)} = 49.5 \text{ kg s}^{-1} \text{ m}^{-3}$), and the exact composition of the feed was determined. Afterwards, the temperature was set to 250 °C (heating rate: 2 °C min^{-1}), and the catalytic performance was measured for 3 h. With steps of 50 °C, the temperature was increased up to 400 °C, and each temperature was held for 3 h. At the

end, the deactivation behavior was determined from CO_2 conversion data using a return point at 300 °C as benchmark (see Eq. (3) in the supplement). Details of the measurement protocol are described in Fig. S7.

The activity of SiC and the reactor steel was investigated in a blank test. No significant conversion could be found at $p_{\text{abs}} = 1.6 \text{ MPa}$ and $T = 400 \text{ }^{\circ}\text{C}$ ($X(\text{CO}_2) < 1\%$). Gas analysis was carried out using gas chromatography (GC, HP 6890) and an NDIR detector (ABB 3020, URAS26). The gas chromatograph was equipped with column switching, where the gas sample was led onto a Hayesep-Q column (separation of H_2O , CO_2 and C_{2+} hydrocarbons) and a molecular sieve column (separation of H_2 , Ar, N_2 , CO, CH_4). The components were detected with a thermal conductivity detector (TCD) and a flame ionization detector (FID). The response factors of the components were determined by external calibration and allowed to calculate the molar amounts in the sample loop. The GC conversion of CO_2 and the selectivity of CO were determined using a bypass experiment with an internal standard according to Eqs. (9) and (10). In order to take the volume contraction into account, about 5 vol.-% of Ar was added as internal standard. Thus, the volume contraction is included through the ratio of the Ar peak area of the bypass experiment $A_{\text{Ar,in}}$ and during the reaction $A_{\text{Ar,out}}$. The carbon balance was closed to $+/- 1\%$.

$$X(\text{CO}_2) = \frac{n_{\text{CO}_2,\text{in}} - n_{\text{CO}_2,\text{out}} \cdot \left(\frac{A_{\text{Ar,in}}}{A_{\text{Ar,out}}} \right)}{n_{\text{CO}_2,\text{in}}} \quad (9)$$

$$S(\text{CO}) = \frac{n_{\text{CO},\text{out}} \left(\frac{A_{\text{Ar,in}}}{A_{\text{Ar,out}}} \right)}{n_{\text{CO}_2,\text{in}} - n_{\text{CO}_2,\text{out}} \cdot \left(\frac{A_{\text{Ar,in}}}{A_{\text{Ar,out}}} \right)} \quad (10)$$

Since the internal standard could not be detected by NDIR, the IR-based conversion of CO_2 was calculated using a balance approach of the molar amounts in the cuvette according to Eqs. (11) and (12). This was possible since the only byproducts detected by gas chromatography were CO and traces of ethane. The conversions determined by gas chromatography and NDIR were in perfect agreement.

$$X(\text{CO}_2) = \frac{n(\text{CH}_4)_{\text{out}} + n(\text{CO})_{\text{out}}}{n(\text{CO}_2)_{\text{out}} + n(\text{CH}_4)_{\text{out}} + n(\text{CO})_{\text{out}}} \quad (11)$$

$$S(\text{CO}) = \frac{n(\text{CO})_{\text{out}}}{n(\text{CH}_4)_{\text{out}} + n(\text{CO})_{\text{out}}} \quad (12)$$

The TOF gives the number of converted molecules per active site per time unit [69]. For the calculation of the TOF according to Eq. (13), it was assumed that each Ni surface atom is an active site,

$$\text{TOF} = \frac{\dot{n}_{\text{CO}_2,\text{in}} \cdot X(\text{CO}_2) \cdot N_A}{Z \cdot t} = \frac{N}{Z \cdot t} \quad (13)$$

with the Avogadro constant N_A , the number of active sites Z , the number of converted molecules N and the time t . The TOF was determined at a constant conversion $X(\text{CO}_2)$ of 30% achieved by adjusting $\dot{n}_{\text{CO}_2,\text{in}}$, thus giving strictly speaking a mean TOF for the concentration range covered by the chosen conversion. Three measurements of the same sample gave a deviation of the TOF value of $\pm 3\%$.

The weight time yield (WTY) and the space time yield (STY) were calculated with Eqs. (14) and (15)

$$\text{WTY} = \frac{\dot{m}_{\text{CH}_4}}{m_{\text{cat}}} \quad (14)$$

$$\text{STY} = \frac{\dot{m}_{\text{CH}_4}}{V_R} \quad (15)$$

with the mass flow of methane \dot{m}_{CH_4} , the catalyst mass m_{cat} and the reactor volume taken by the catalyst without inert material V_R . The reactor volume of the undiluted catalyst was determined using the bulk

density of the catalyst. For the determination of the bulk density, a calibration curve was recorded using a graduated cylinder with the diameter of the reactor.

3. Results and discussion

3.1. Metal loading

The measured Ni loadings (the percentage of the Ni mass fraction) are contained in the sample designation (precise values are given in Table S6). A significant Na mass fraction is observed for the samples 20DP, 51CP, 57CP and 65CP. The higher Na mass fraction of the 20DP sample is probably due to the fact that this sample was washed with less demin. water than the other DP samples (see Section 2.1.). For the CP samples, the Na mass fraction decreases with increasing $n_{\text{Ni}}/n_{\text{Al}}$. Since all CP samples were washed with the same amount of demin. water, the different Na contents indicate that it becomes increasingly difficult to remove the Na^+ ions with decreasing $n_{\text{Ni}}/n_{\text{Al}}$. The sodium content of the 51CP samples is significantly larger than the one of the other CP samples. It is shown in the XRD investigation (see Section 5. in the supplement) that only in the 51CP sample pure aluminum hydroxide components are formed. Hence, we assume that Na^+ ions are adsorbed by the aluminum hydroxide components [61], which explains the higher Na content of the 51CP sample.

3.2. N_2 physisorption

For the production of highly loaded $\text{Ni-Al}_2\text{O}_3$ catalysts, information on textural changes with increasing Ni mass fraction w_{Ni} is important and monitored with N_2 physisorption (isotherms are given in Figs. S1–S4). It is obvious that the measured BET surface area of all supported catalysts decreases nearly linearly with increasing w_{Ni} (Fig. 1, filled symbols). This behavior is often explained with a negative influence of the metal loading on the texture [51] (e.g., blocking of pores [35,51,70]). However, the decrease can rather be explained with the fact that the mass fraction of the porous $\gamma\text{-Al}_2\text{O}_3$ support decreases with increasing w_{Ni} [71]. This interpretation is supported by the fact that the modified BET surface area $S(\text{BET})_{\text{mod}}$, i.e., the BET surface area related to the support mass as calculated with Eq. (2), does not change significantly (open symbols). The small $S(\text{BET})_{\text{mod}}$ values of the samples 81WI and 88WI can be due to an inaccurate measurement, since there is only 12–19% of support left in the samples. If Ni were completely deposited in the pores of 81WI and 88WI, Ni would fill 88% and 100% of the pore volume.

A similar behavior can be observed for the pore volumes: The measured pore volumes of the WI and the DP samples decrease linearly with increasing Ni mass fraction w_{Ni} (filled symbols). If the pore volume is related to the support mass using Eq. (3), the modified pore volume $V_{p,\text{mod}}$ is very similar to the one of the pure support (open symbols). For the DI samples, the decrease of the measured pore volume V_p is up to $w_{\text{Ni}} = 30\%$ much more significant than for the other supported catalysts. Even if the values are related to the support mass, the modified pore volumes $V_{p,\text{mod}}$ of samples 14DI, 25DI and 30DI are smaller than the one of the pure support. For the CP samples, the porosity is not due to a support but forms only during the thermal treatment of the precipitated samples [72]. Thus, only measured but no modified BET surface areas and pore volumes can be given for the CP samples, and the corresponding values are larger than the ones of the supported catalysts with similar w_{Ni} .

Thus, these results show that the Ni loading affects the texture of the support only significantly in samples 14DI, 25DI and 30DI. For a more detailed investigation of the texture, the pore size distribution was calculated with the BJH method (Fig. 2). For the supported catalysts, only the $\gamma\text{-Al}_2\text{O}_3$ support should have mesopores, and thus, only the support content should have an influence on the pore size distribution. The actual values of the pore size distribution should depend on the

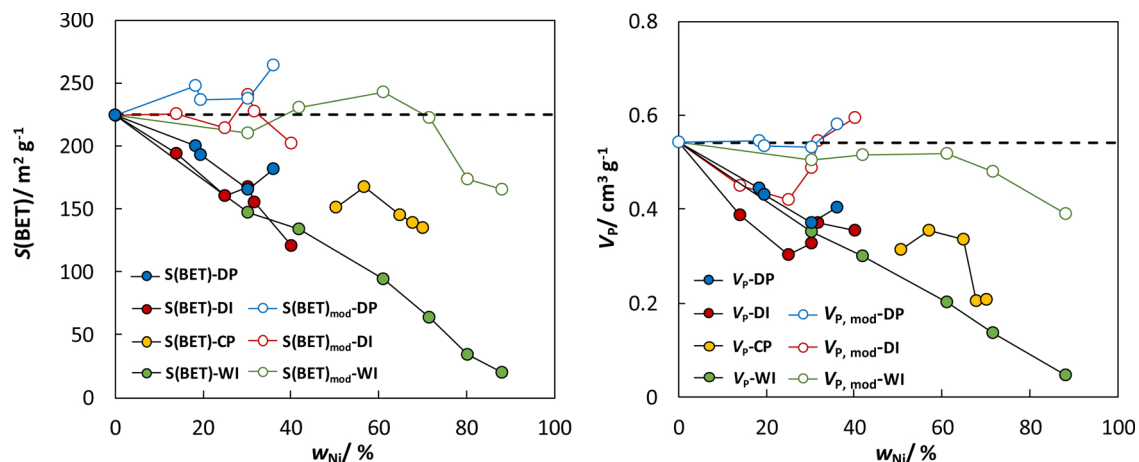


Fig. 1. BET surface areas $S(\text{BET})$ and pore volumes V_p of the reduced and passivated samples in dependence of the Ni mass fraction w_{Ni} . Dashed line: value of the calcined support. Measured values are given as $S(\text{BET})$ and V_p ; values related to the support mass were calculated with Eqs. (2) and (3) and named with $S(\text{BET})_{\text{mod}}$ and V_p, mod (only supported catalysts).

composition of the sample, whereas the shape of the pore size distribution should give hints on the texture of the support.

The shape of the pore size distributions of the WI samples does not significantly depend on the Ni loading. Thus, the BET surface areas, the pore volumes and the pore size distributions consistently show that the Ni loading has no significant effect on the support texture, even though w_{Ni} increases from 30 to 88%. Thus, we assume that the larger fraction of the Ni does not reach the support pores and that the Ni amount in the pores is similar for all samples. Hence, the Ni amount which reaches the pores is independent from the Ni loading and the initial Ni^{2+} concentration of the impregnation solution. Only a detailed look at the catalyst preparation can explain this: Due to the vaporization of the water, the concentration of the dissolved $\text{Ni}(\text{NO}_3)_2$ increases, until the saturation concentration is exceeded, at which point $\text{Ni}(\text{NO}_3)_2 \cdot x\text{H}_2\text{O}$

starts to precipitate in the solution and on the external surface of the support. Afterwards, the water in the pores starts to vaporize, and $\text{Ni}(\text{NO}_3)_2 \cdot x\text{H}_2\text{O}$ starts to precipitate in the pores. Thus, the Ni amount in the pores is limited by the saturation concentration and independent of the Ni loading and the initial Ni^{2+} concentration of the impregnation solution which explains why the support texture does not change significantly with the Ni loading.

By contrast, the shape of the pore size distribution does change with the Ni loading for the DI samples, which shows that Ni reaches the support pores during dry impregnation. A comparison with the pure support shows for the samples 14DI, 25DI and 30DI a significant decrease of pores larger than 7 nm and a small increase of pores smaller than 7 nm, which can be explained with the fact that Ni reduces the mesopore diameter. This also explains why the modified BET surface

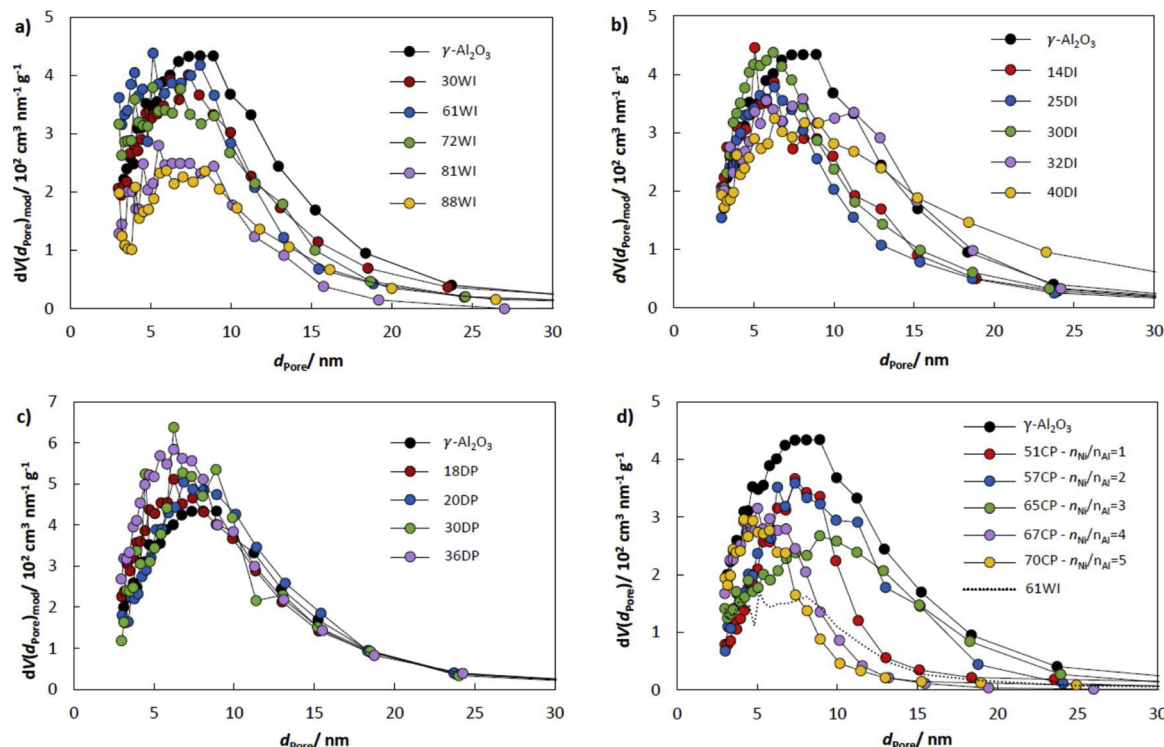


Fig. 2. Pore size distributions calculated from the adsorption branch of the reduced and passivated a) WI, b) DI, c) DP samples related to the support mass, respectively, and d) CP samples related to the catalyst mass.

area of the samples 14DI, 25DI and 30DI stays constant, even though the modified pore volume decreases (Fig. 1): Due to the decrease of the proportion of larger pores and the increase of the proportion of smaller pores, the surface/volume ratio increases, which keeps the modified BET surface area constant with decreasing modified pore volume. The pore size distribution of 32DI is similar to the one of the pure support, but with a smaller proportion of pores < 11 nm. The sample 40DI shows a higher proportion of pores > 15 nm which results in a broader pore size distribution as compared to the support. The significant difference between the samples 14DI to 30DI and 32DI to 40DI is presumably due to the fact that the impregnation solution for the last impregnation step was less concentrated for the samples 32DI and 40DI (see Table S3 and further discussion in Section 3.5), which shows that the concentration of the impregnation solutions has a significant influence on the Ni distribution.

For the DP samples, there is hardly any change of the pore size distribution with increasing Ni loading, which could be explained by the fact that nickel hydroxide already precipitates in the solution and does not reach the pores of the support. If we assume that the Ni precursor reaches the support pores, we have to postulate for a constant support texture a high dispersion and a homogeneous distribution of the Ni precursor. Would the Ni precursor precipitate at certain positions within the pores, the pore size distribution should change. With further characterization results, we will show that no nickel hydroxide precipitates in solution and that indeed a high Ni dispersion is obtained with the DP samples.

For the CP samples, the pore size distribution changes significantly with changing $n_{\text{Ni}}/n_{\text{Al}}$. The larger BET surface areas and the larger pore volumes of 57CP and 65CP can be explained with the pore size distributions as compared to the supported catalysts. If $\gamma\text{-Al}_2\text{O}_3$ is impregnated with Ni, the support mass fraction decreases linearly with increasing Ni loading. Due to the decreasing support mass fraction, the pore density also decreases (exemplarily shown in Fig. 2d) for 61WI, dotted line; note that the numbers of 61WI are different in Fig. 2a) and d), since the values in Fig. 2a) are related to the support mass, and the values in Fig. 2d) are related to the catalyst mass). Since the pore density of the CP samples is significantly higher than the one of the supported catalysts at the same Ni loading, a higher BET surface area is obtained. The 57CP sample has the highest BET surface area and the highest pore volume of all CP samples, since this sample has a high proportion of both, small (< 10 nm) and large pores (> 10 nm). The 65CP sample shows a pore volume similar to the one of the 57CP sample, since the proportion of pores > 10 nm is similar. However, the BET surface area of 65CP is smaller, since the proportion of smaller pores is smaller than for 57CP. The samples 51CP, 67CP and 70CP reach a BET surface area similar to the one of 65CP, even though the pore volume is smaller. This is possible, since these samples have a high proportion of smaller pores, whereby a large surface/volume ratio is achieved. Thus, the analysis of the pore size distribution shows clearly, that the texture of the CP samples changes with changing $n_{\text{Ni}}/n_{\text{Al}}$ ratio.

3.3. X-ray diffraction (XRD)

For a quantification of the peak widths, the mean crystallite sizes \bar{d}_c were calculated by the Scherrer Eq. (Fig. 3). For the WI samples, the NiO crystallite size increases fairly regularly with increasing w_{Ni} , whereas the NiO crystallite size of the DI samples jumps up from a Ni mass fraction of 30% on. The NiO crystallite size of the DP samples is nearly independent of w_{Ni} .

The Ni crystallite size of the WI and DI samples increases with increasing w_{Ni} with a smaller slope than the NiO crystallite size. The Ni crystallite size of the DP and CP samples seems to be independent of the Ni loading. It is noticeable that the NiO and the Ni crystallite sizes only differ significantly, if there are large NiO crystallites. If the NiO crystallite size is < 10 nm, the NiO and the Ni crystallite sizes are very similar (26DI, 30DI, 30DP, 36DP; for 14DI, 18DP and 20DP, the NiO

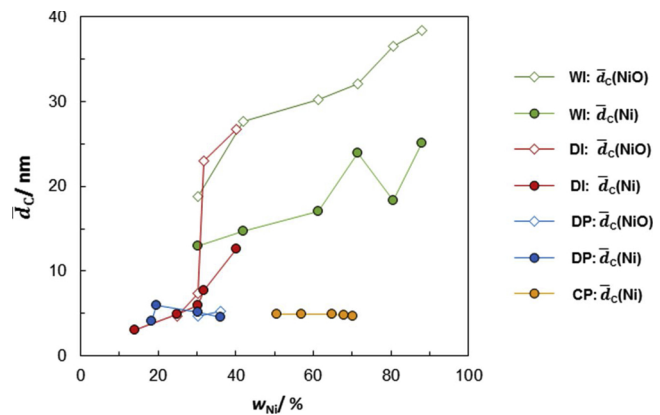


Fig. 3. Comparison of the mean NiO and Ni crystallite sizes from XRD data (for details see Section 5. and Figs. S5 and S6 of the Supplementary data) of calcined and reduced samples.

reflections are too weak for a meaningful evaluation). The difference between the crystallite sizes of NiO and Ni is discussed in greater detail in Section 3.6.

3.4. Temperature-programmed reduction (TPR)

For a further identification of the different Ni species, TPR measurements were conducted. We start with the 14DI sample, since this sample has the least complex TPR profile with only difficult-to-reduce Ni species (Fig. 4a)). By deconvolution, the TPR profile can be divided into three reduction peaks: The reduction peak at 760 °C is in the temperature range of crystalline nickel aluminate (750–950 °C [73]). However, XRD does not point to crystalline nickel aluminate (see Section 5. in the supplement). Wu and Hercules [74] show that Ni^{2+} ions can diffuse into the octahedral and tetrahedral voids of the $\gamma\text{-Al}_2\text{O}_3$ surface. The Ni^{2+} ions in the tetrahedral voids are more difficult to reduce than the ones in the octahedral voids. Hence, we assume that the reduction peak at 760 °C is caused by Ni^{2+} ions in the tetrahedral voids and the reduction peak at 560 °C by Ni^{2+} ions in the octahedral voids, which are subsequently denoted as $\text{T}(\text{Ni}^{2+})$ and $\text{O}(\text{Ni}^{2+})$ species, respectively. With XRD, the $\text{Al}(\text{Ni})\text{O}_x$ structure of the $\text{T}(\text{Ni}^{2+})/\text{O}(\text{Ni}^{2+})$ species cannot be observed, since there is only one atomic layer of this structure [75]. The reduction peak at 460 °C is presumably caused by the reduction of NiO. If the octahedral and the tetrahedral voids of spinel-type $\text{Al}(\text{Ni})\text{O}_x$ at the surface are filled, crystalline NiO is formed [41,75]. The weak NiO peak of the 14DI sample points to the fact that the tetrahedral and octahedral voids are not yet completely filled. With the samples 25DI to 40DI, the proportion of the NiO peak increases with increasing Ni loading (Fig. 4b)), and at the same time, more distinct NiO reflections appear in the diffractograms, which supports the assumption that the TPR peak at 460 °C is caused by NiO.

As a reference for pure NiO, a NiO standard was prepared after the method of Richardson and Twigg [76]. The reduction peak of this NiO standard at temperatures between 290 and 340 °C is relatively narrow. The NiO species of the DI samples are more difficult to reduce than this NiO standard. Since smaller NiO particles are more difficult to reduce [48,75], the lower reducibility could be explained with the fact that the NiO particles are bound to the support surface and are smaller than the ones of the NiO standard. In addition, an interaction with the support which impedes the reduction is conceivable. These NiO species bound to the support are, hence, in the following denominated with B(NiO), where the “B” indicates bound NiO. Thus, the TPR investigation shows that an increase of the Ni loading of the DI samples leads to a higher proportion of crystalline NiO bound to the support. All DI samples show a small peak at around 270 °C, which could be due to the reduction of easily reducible oxygen atoms on the NiO surface. Yang et al. speculate

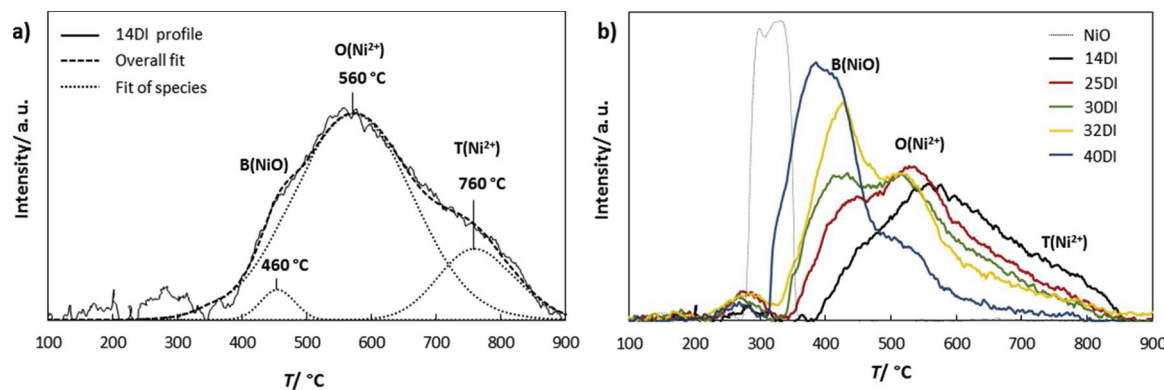


Fig. 4. TPR profiles of the calcined DI samples and the squeezed profile of the NiO standard. Denominated species: B(NiO): NiO bound to the support, O(Ni²⁺): Ni²⁺ ions in octahedral voids, T(Ni²⁺): Ni²⁺ ions in tetrahedral voids of spinel-type Al(Ni)O_x.

that it is easier to reduce amorphous NiO than crystalline NiO [77] so that this peak could be due to amorphous NiO. However, it could also be due to traces of Ni₂O₃, since Ho and Chou show that Ni₂O₃ is more easily reducible than NiO [78].

The TPR profiles of the WI samples are more complex (Fig. 5). The profile of 30WI contains a narrow reduction peak at 330 °C and a significantly broader reduction peak at higher temperatures. The broader reduction peak agrees with the TPR profile of the 30DI sample (shown with the dotted line in Fig. 5), for which reason it is presumably caused by the already assigned B(NiO), O(Ni²⁺) and T(Ni²⁺) species. Since the additional reduction peak is located in the range of the NiO standard, we assume that it is caused by unsupported NiO particles, which is why this species is denominated with F(NiO), where the “F” indicates free NiO. The reduction of the NiO standard starts already at somewhat lower temperatures, since the NiO standard probably consists of larger particles, which can be more easily reduced. It is interesting that an increase of the Ni loading leads only to an increase of the F(NiO) species, whereas the proportion of the other species (B(NiO), O(Ni²⁺) and T(Ni²⁺)) decreases. Through the increase of the proportion of the F(NiO) species, these species overlap with the B(NiO) species in the samples 42WI to 72WI, for which reason the maximum of the F(NiO) peaks is shifted to higher temperatures.

For the samples with a higher Ni loading, 81WI and 88WI, a striking difference to the samples with a lower Ni loading is another reduction peak with Lorentzian profile at 250 °C, which points to an exothermic reduction, for which reason we assume that the reduction peak is caused by unconverted Ni(NO₃)₂·xH₂O [43]. At a Ni mass fraction $\geq 81\%$, the calcination is, hence, insufficient to completely convert the Ni

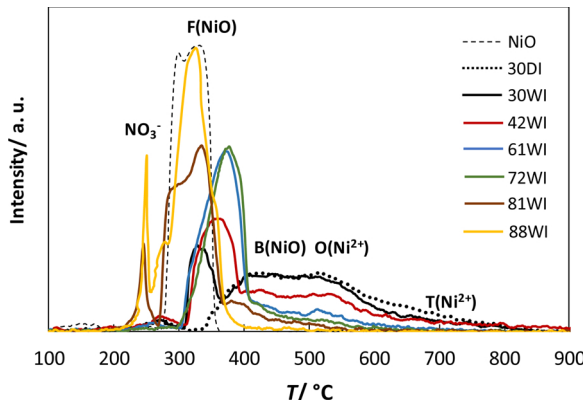


Fig. 5. TPR profiles of the calcined WI samples and the squeezed profile of the NiO standard, as compared to the 30DI sample (dotted line). Denominated species: F(NiO): free, unsupported NiO, B(NiO): NiO bound to the support, O(Ni²⁺): Ni²⁺ ions in octahedral voids, T(Ni²⁺): Ni²⁺ ions in tetrahedral voids of spinel-type Al(Ni)O_x.

(NO₃)₂·xH₂O precursor ($T_{\text{calc.}} = 400$ °C, $t_{\text{calc.}} = 3$ h), probably because larger precursor particles are formed [78]. It is further noticeable that the F(NiO) peak has a shoulder at 280 °C. Ho and Chou show that this shoulder is caused by the reduction of Ni₂O₃, which forms during the reduction of Ni(NO₃)₂·xH₂O [78].

In Section 3.2, we assumed that the Ni amount in the pores is constant and that an increase of the Ni loading only leads to an increase of unsupported F(NiO). This assumption can now be verified with the TPR investigation. On the support, the Ni is present as B(NiO), O(Ni²⁺) and T(Ni²⁺). A deconvolution of the TPR profile of 30WI yields a percentage of about 23% B(NiO), O(Ni²⁺) and T(Ni²⁺) species, and the same holds for 42WI. At higher Ni loadings, a reliable estimate of B(NiO) is, due to the overlap with F(NiO), not possible, even though the value should decrease, since the mass fraction of the support decreases. Hence, the TPR investigation supports the assumptions made on the basis of the N₂ physisorption results.

For an investigation of the influence of the preparation method and the Ni loading on the formation of the T(Ni²⁺) and O(Ni²⁺) species, the NiO mass is related to 100 m² BET surface area of the support and denoted with $m(\text{NiO})^*$. In Fig. 6, the NiO mass per support surface area is plotted against the Ni mass fraction (circle symbol). The percentage of the T(Ni²⁺) and O(Ni²⁺) ratio is determined with deconvolution of the TPR profiles. A multiplication of this percentage with the NiO mass per support surface area gives a constant value (diamond symbol; ≈ 0.16 g NiO per 100 m² γ -Al₂O₃). Only for the sample with the lowest Ni loading (14DI), a lower value is obtained. It has already been assumed

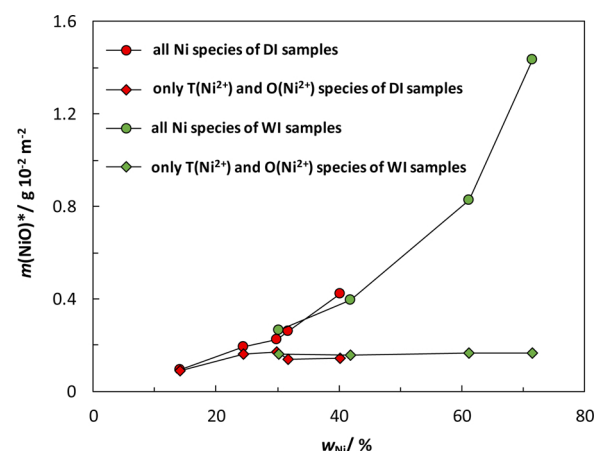


Fig. 6. NiO mass of the calcined samples 14DI to 40DI and 30WI to 72WI related to 100 m² BET surface area S(BET) (denoted with $m(\text{NiO})^*$) of all Ni species (symbol: circle) or of only the T(Ni²⁺) and O(Ni²⁺) species as determined by deconvolution of TPR data (symbol: diamond) plotted against the Ni mass fraction of the reduced and passivated samples.

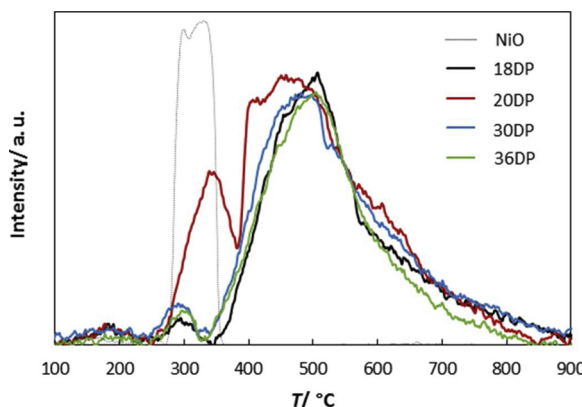


Fig. 7. TPR profiles of the calcined DP samples and the squeezed profile of the NiO standard.

above that the tetrahedral and octahedral voids of the 14DI sample are not completely filled, which is thus supported by Fig. 6.

Therefore, the discussion shows that the impregnation method and the Ni loading do not have an influence on the percentage of the $T(Ni^{2+})$ and $O(Ni^{2+})$ species. With both impregnation methods, a Ni loading of up to 0.16 g NiO per 100 m² can be dispersed atomically (corresponding to 12.5 Ni²⁺ ions per nm², the conversion of the numbers is explained in the supplementary data, Eq. (1)). The maximum of atomically dispersed metal ions can be named dispersion capacity [79]. After the incorporation model, the γ -Al₂O₃ surface possesses 9–9.8 octahedral and tetrahedral voids per nm², which are accessible for the Ni²⁺ ions [75]. The value measured in this study for the $T(Ni^{2+})$ and $O(Ni^{2+})$ species is, thus, with 12.5 Ni²⁺ ions per nm² only slightly higher than the value of the incorporation model. Thus, the discussion shows that the assumption of the percentage of the $T(Ni^{2+})$ and $O(Ni^{2+})$ species is supported by theoretical considerations.

In the TPR profiles of the DP samples, there is a significant difference between 20DP and the other DP samples (Fig. 7). 20DP was washed with less water and has a Na mass fraction of 2.2% as compared to values of $\leq 0.4\%$ for the other samples (Table S6). The additional reduction peak of 20DP at 340 °C is in the range of the NiO standard and is probably due to free NiO (F(NiO)). During deposition precipitation, there is the danger that a short-time pH gradient occurs during the dropwise addition of NaOH which can lead to the precipitation of pure Ni(OH)₂ [80]. Ni(OH)₂ is converted into F(NiO) during calcination. Thus, the additional reduction peak of 20DP points to the precipitation of unsupported Ni(OH)₂, which might have been washed away with the higher volume of washing water for the other DP samples (18DP, 30DP, 36DP). In Section 3.2, it was considered that the support texture does not change because Ni(OH)₂ precipitates in solution. This possibility can now be excluded with the TPR investigation, since pronounced F(NiO) species are only present in 20DP. The very weak reduction peaks at 300 °C show that there are only traces of NiO in the samples 18DP, 30DP and 36DP.

The TPR profiles of the samples 18DP, 30DP and 36DP show only one broad peak which does not change with increasing Ni loading which means that only a larger amount of the same Ni species is formed. Since always the same Ni amount is placed in the TPR tube, the increase of the amount cannot be observed in Fig. 7. The maximum of the reduction peak of the DP samples is in the range of the $O(Ni^{2+})/T(Ni^{2+})$ species. It has been shown above that the maximal amount of the $T(Ni^{2+})/O(Ni^{2+})$ species is limited by the amount of octahedral and tetrahedral voids in the γ -Al₂O₃ surface (≈ 0.16 g NiO per 100 m²). The reduction peak does not change, even though this maximum is clearly surpassed (30DP: 0.23 g NiO per 100 m²; 36DP: 0.25 g NiO per 100 m²). Therefore, we can assume that a different Ni species is responsible for the peak. In Section 5. in the supplement, a Ni(Al)O_x species was observed in the X-ray diffractogram of 30DP and 36DP. It is well known

that it is much more difficult to reduce NiO, if Al³⁺ ions are included in the NiO lattice [75,81]. Therefore, we would call this species doped NiO (D(NiO)).

If we assume that Ni reaches the pores of the support without changing the support texture, Ni must be distributed homogeneously with high dispersion. Furthermore, it is noticeable that most DP samples do not show NiO, even though there are significant proportions of B(NiO) and F(NiO) species in the WI and DI samples with similar Ni loadings. During deposition precipitation, Ni is deposited on the support surface as hydrotalcite-like layered double hydroxides (takovite) [82], and Ni²⁺ ions are coordinated to the hydroxyl groups of the γ -Al₂O₃ surface in the interface area takovite- γ -Al₂O₃. The number of these hydroxyl groups is about 18 OH per nm², whereas the amount of the tetrahedral and octahedral voids in Al(Ni)O_x is only about half as much (9.0–9.8 voids per nm²) [75]. Thus, the adsorption capacity of deposition precipitation could be twice as large as the dispersion capacity of the impregnation methods. The value of 21 Ni²⁺ ions per nm² (sample 36DP) agrees well with the number of hydroxyl groups. However, the hydrotalcite-like layered double hydroxides should have an interlayer distance of $c_0 = 0.78$ nm, which is why for steric reasons not on each OH group a double hydroxide layer can form [82]. Since multilayer adsorption of Ni²⁺ ions is possible, the high value can be caused by multilayer adsorption [82]. Thus, the discussion shows that during deposition precipitation large amounts of Ni²⁺ ions can be deposited on the surface due to the high amount of hydroxyl groups and the possibility of multilayer adsorption. Due to the high adsorption capacity, the Ni²⁺ ions are even at high Ni loadings completely deposited as hydrotalcite-like precursors. During a controlled addition of the OH[−] ions, the surface of the γ -Al₂O₃ support should first be completely covered with the hydrotalcite-like species, before Ni(OH)₂ is formed. Thus, the Ni is even at high Ni loadings distributed with high dispersion on the support surface.

The CP samples were investigated by TPR as dried, not calcined precipitation products (Fig. 8). Thus, also the thermal decomposition of the layered double hydroxides occurs during the temperature-programmed reduction. This thermal decomposition is to a large part completed already below 330 °C [55].

Therefore, we assume that the reduction peaks are rather caused by oxidic (Ni(Al)O_x) and not by hydroxidic (takovite) Ni species. All CP samples show a weak reduction peak at 350 °C, which is probably due to the reduction of surface oxygen or a small amount of NiO. There is no significant amount of NiO, even at high Ni loadings. Thus, the Ni²⁺ ions are completely inserted into the double hydroxide layers and are mixed with Al³⁺ ions. At around 400 °C, there is a narrow and intensive peak which overlaps with a broad peak at higher temperatures. Samples 51CP to 65CP show a shoulder around 600 °C, which could be due to the presence of Al(Ni)O_x species or a Ni(Al)O_x species with high Al³⁺

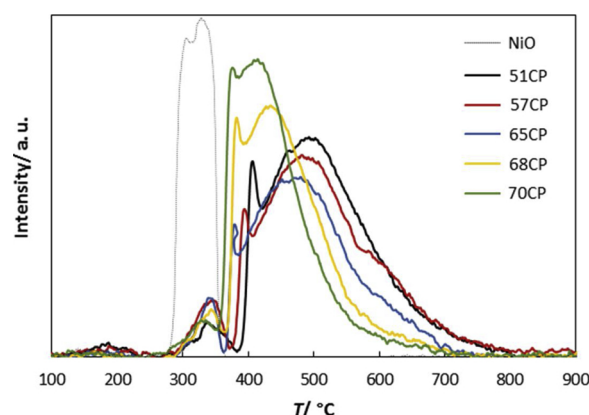


Fig. 8. TPR profiles of the dried CP samples and the squeezed profile of the NiO standard.

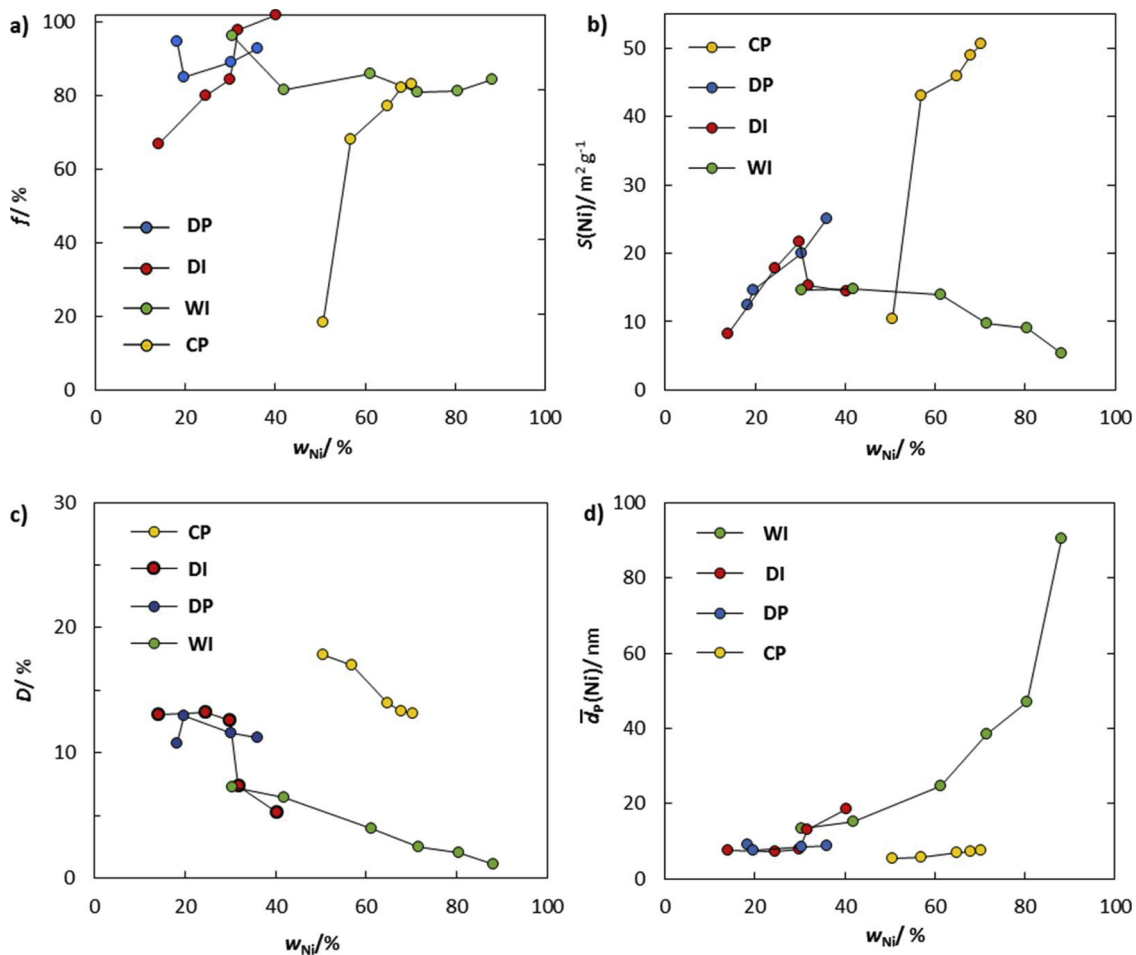


Fig. 9. a) Extent of reduction f , b) Ni surface area $S(Ni)$ related to the mass of the pre-reduced and passivated catalyst, c) Ni dispersion D and d) mean particle size $\bar{d}_p(Ni)$ of the different samples.

percentage (similar to the DP samples) which are difficult to reduce. Both peaks shift to lower temperature with increasing n_{Ni}/n_{Al} , and the broader peak becomes narrower. It is known that it is more difficult to reduce $Ni(Al)O_x$ species, if the Al^{3+} proportion increases [81], which shows that the observed shift of the peaks is due to the decreasing share of Al^{3+} in the $Ni(Al)O_x$ species with increasing n_{Ni}/n_{Al} ratio. Thus, the TPR and the XRD investigations show that only $Ni(Al)O_x$ species with different proportions of Al^{3+} are formed in the CP samples.

3.5. H_2 chemisorption

For the calculation of the metal dispersion and the particle size, we have to know, besides the adsorbed amount of H_2 determined by H_2 chemisorption, the amount of metallic Ni. This latter amount is obtained by measuring the extent of reduction with thermogravimetry. For the DI, DP and CP samples, the extents of reduction (Fig. 9a)) agree with the expectations from temperature-programmed reduction. The extent of reduction increases for the DI samples with increasing Ni mass fraction w_{Ni} , since the share of the $B(NiO)$ species increases, which are more easily reduced. The DP samples have high extents of reduction between 85 and 95% and show no visible dependence on w_{Ni} . This confirms the TPR results, since a large part of the Ni is already reduced below 600 °C and the reduction peak does not change with increasing w_{Ni} . The difference in the extents of reduction of 51CP and 57CP is larger than expected from the TPR profiles. However, the following has convinced us that the measured extent of reduction of 51CP is correct: 1) The NiO reflections of reduced 51CP are significantly stronger than the ones of 57CP (Fig. S6). 2) The ratio of the reflection intensities I

(Ni)/ $I(NiO)$ is much smaller for 51CP than for 57CP. 3) After reduction of 51CP at 400 °C for 3 h instead of 1 h, the extent of reduction has increased by a factor of 1.6 (Section 3.10). The extent of reduction increases significantly with increasing w_{Ni} of the other CP samples. This is expected according to the results from TPR and XRD, since, with increasing w_{Ni} and increasing n_{Ni}/n_{Al} , the share of Al^{3+} in the $Ni(Al)O_x$ species decreases, which increases the reducibility.

Contrary to the expectations, the extent of reduction for the WI samples 42WI to 88WI is between 81% and 87%. At $w_{Ni} > 61\%$, the main Ni species is the easily reducible $F(NiO)$, why we would expect an extent of reduction of nearly 100%. However, it is observed with thermogravimetry that the Ni particles of the WI samples are oxidized more slowly than the particles of the other samples. This can be explained with the fact that during wet impregnation large unsupported Ni particles are formed, which could be more difficult to oxidize so that the thermogravimetrically determined extent of reduction might underestimate the actual extent of reduction. Therefore, also a longer oxidation time was chosen for the WI samples (see Section 2.2).

The Ni surface area, the Ni dispersion and the mean Ni particle size (Fig. 9) were determined with H_2 chemisorption. For the WI samples, the Ni particle size increases moderately up to a w_{Ni} of 61% ($\bar{d}_p(Ni) = 13–25$ nm), so that the Ni surface area stays nearly constant. This shows that the lower surface/volume ratio of the larger particles is balanced with the increasing Ni loading. With a further increase of the Ni content, the particle size increases significantly, and the Ni surface area and the dispersion decrease considerably, which shows that, at these high Ni loadings, the smaller surface/volume ratio of the larger particles cannot be balanced any more with the larger Ni loading.

For the DI samples, the Ni particle size and the dispersion are nearly constant up to a w_{Ni} of 30%, which means that an increase of w_{Ni} leads to a larger number of equally sized particles. Due to the higher number of equally sized particles, the Ni surface area increases linearly with w_{Ni} . With 32DI, the properties change abruptly: The Ni particles become considerably larger, so that the Ni surface area and the dispersion decrease. The last impregnation step for 32DI and 40DI was carried out with a less concentrated impregnation solution in order to adjust the Ni content to predefined values (Table S3). Possibly, the small $Ni(NO_3)_2 \cdot xH_2O$ particles are dissolved in the less concentrated impregnation solution, and larger particles are formed outside the mesopores on the external surface of the support. This assumption is supported by the results of N_2 physisorption (Section 3.2).

The DP samples have a nearly constant Ni particle size and dispersion with increasing w_{Ni} , which leads to a linear increase of the Ni surface area up to the high w_{Ni} value of 36%. This means that an increase of w_{Ni} leads to a higher number of equally sized particles.

For the CP samples, the particle size increases only slightly with increasing w_{Ni} ($\bar{d}_p(Ni) = 5–7$ nm). Even at the high w_{Ni} value of 70%, a particle size of 7 nm is obtained. Due to the small extent of reduction, 51CP has a small Ni surface area, in spite of the small particle size. Through the strongly increasing extent of reduction and the small increase of the particle size, the Ni surface area increases strongly with increasing w_{Ni} , whereas the dispersion decreases.

If we compare the Ni surface areas of the different samples, it becomes obvious that out of the supported catalysts 36DP and out of the coprecipitated catalysts 70CP have the largest Ni surface areas. In the literature, a maximum metal surface area of $50\text{ m}^2\text{ g}^{-1}$ is reported with coprecipitated catalysts [83]. Thus, the Ni surface area of 70CP is with $51\text{ m}^2\text{ g}^{-1}$ in the range of the literature value and clearly outperforms the values of the supported catalysts. Hence, deposition precipitation and coprecipitation are the best methods for the preparation of catalysts with a high Ni surface area.

3.6. Distribution of the Ni on the supported catalysts

The aim of the catalyst development is the increase of the weight time yield or the space time yield of the catalysts. For a structure-sensitive reaction, catalysts with a maximum number of small metal particles should be synthesized. In a structure-insensitive reaction, only the metal surface of the catalysts is decisive. There are several possibilities to increase the particle number and the metal surface: On the one hand, it can be attempted to increase the metal dispersion by an appropriate preparation method. On the other hand, the metal loading can be increased. In general, it is assumed that an increase of the metal loading leads to larger particle diameters and a decrease of the metal dispersion [44,45,47–49]. The change of the metal surface with increasing metal loading depends on the increase of the particle size. For a knowledge-based development of Ni catalysts with a very high weight time yield, it is, hence, important to understand the parameters determining the particle size. For an investigation of the influence of the surface chemistry, the Ni surface area per support surface is plotted versus the NiO mass per support surface denoted with $m(NiO)^*$ (Fig. 10). This plot helps to compare the Ni surface area with the results of the TPR investigation, which shows the influence of the different Ni species on the Ni surface area.

In Section 3.4, the Ni dispersion capacity in alumina was determined with TPR ($0.16\text{ g NiO per }100\text{ m}^2 \gamma\text{-Al}_2\text{O}_3$). This value is given in Fig. 10 as dashed line. Since the surface of the catalysts is mainly due to the mesopores, the Ni of the $O(Ni^{2+})/T(Ni^{2+})$ species should be completely located in the mesopores. For 14DI, the dispersion capacity is not yet surpassed, which means that all the Ni should occur as $O(Ni^{2+})/T(Ni^{2+})$ species. For 25DI and 30DI, the dispersion capacity is surpassed. XRD and TPR show that the additional Ni is existent as NiO on the support. Fig. 9 shows that the formation of NiO has no influence on the particle size, since the Ni particle sizes of 14DI, 25DI and 30DI

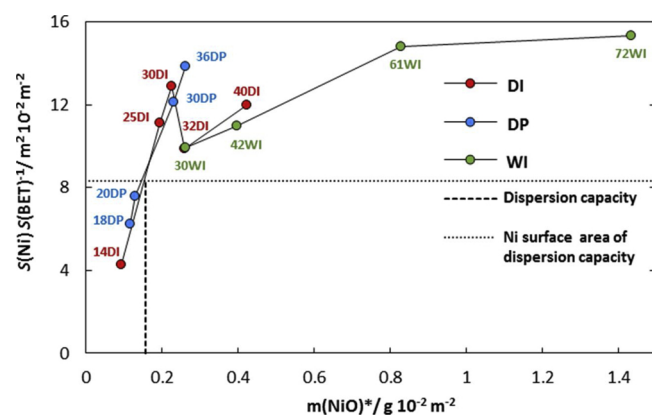


Fig. 10. Ni surface area $S(Ni)$ per 100 m^2 support surface area plotted versus NiO mass per 100 m^2 support surface area denoted with $m(NiO)^*$.

are very similar. Hence, we can assume that the NiO particles formed have roughly the same size as the Ni particles of 14DI, and this assumption can be checked with the XRD results: The $T(Ni^{2+})/O(Ni^{2+})$ species do not lead to visible NiO peaks, since there is only an atomic layer of the $Al(Ni)_O_x$ structure. Hence, the NiO reflections can be seen as a direct measure for the additional NiO crystallites, and the NiO crystallite size is comparable to the Ni particle size of the 14DI sample (25DI and 30DI: $\bar{d}_c(NiO) = 5–7$ nm, Section 3.3., Fig. 3; 14DI: $\bar{d}_p(Ni) = 7$ nm, Section 3.5., Fig. 9). Hence, the NiO crystallites have roughly the same size as the Ni particles of the $T(Ni^{2+})/O(Ni^{2+})$ species (Fig. 11). The increasing Ni loading leads to a larger number of equally sized Ni particles, which is why the Ni surface area increases linearly, even if the dispersion capacity is surpassed (Fig. 10). Since the Ni particle size does not change, the Ni surface area at the dispersion capacity can be interpolated, and the Ni surface area of the $T(Ni^{2+})/O(Ni^{2+})$ species should have a value of 8.3 m^2 per $100\text{ m}^2 \gamma\text{-Al}_2\text{O}_3$ at the dispersion capacity (Fig. 10, dotted line).

For the DP samples, a comparable increase of the Ni surface with increasing Ni loading is observed (Fig. 10), because the particle size is up to $w_{Ni} = 30\%$ very similar for the DP and the DI samples (DP: $\bar{d}_p(Ni) = 8–9$ nm; DI: $\bar{d}_p(Ni) = 7–9$ nm; Fig. 9). Thus, it is noticeable that

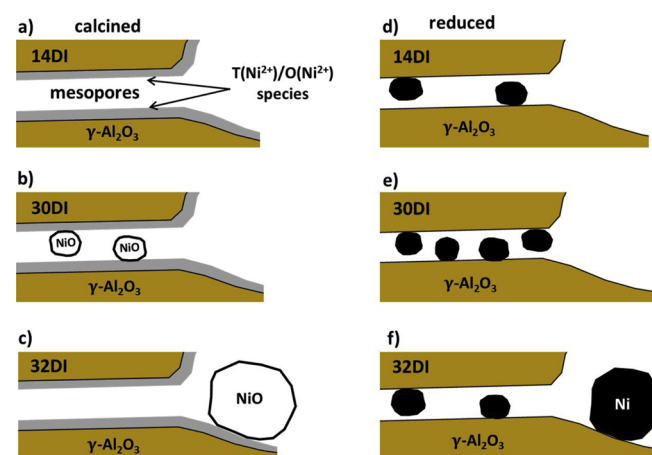


Fig. 11. Scheme of the Ni distribution and the resulting particle size of calcined (a, b) and (c) and reduced (d, e) and (f) samples. a) 14DI: $T(Ni^{2+})/O(Ni^{2+})$ species are mainly located in the mesopores; b) 30DI: besides $T(Ni^{2+})/O(Ni^{2+})$ species, NiO particles are located in the mesopores; c) 32DI: NiO particles are located outside the mesopore system; d) 14DI: Ni particles inside the mesopores formed from $T(Ni^{2+})/O(Ni^{2+})$ species; e) 30DI: Ni particles inside the mesopores formed from NiO particles and $T(Ni^{2+})/O(Ni^{2+})$ species; f) 32DI: Ni particles formed inside the mesopores from $T(Ni^{2+})/O(Ni^{2+})$ species and outside the mesopores from NiO particles.

a very similar Ni particle size is obtained over a wide range of w_{Ni} (14–36%) with different preparation methods (dry impregnation, deposition precipitation). This means that the Ni particle size is independent of the Ni loading, the preparation method and the Ni species ($\text{O}(\text{Ni}^{2+})/\text{T}(\text{Ni}^{2+})$, $\text{B}(\text{NiO})$, $\text{Ni}(\text{Al})\text{O}_x$). Therefore, there must be a parameter which limits the particle size, and this is the mean pore diameter of the support which coincides with the particle size. Hence, we assume that the NiO and the Ni particles are stabilized in the mesopores. Kuo et al. and Bartholomew also assume in an investigation on the deactivation of Ni catalysts that the Ni particles are stabilized once the Ni particle diameter reaches the size of the pore diameter [84,85]. Furthermore, we assume in this work that the structure relationship between the support texture and the Ni particles has a decisive influence already during the preparation and the activation of the samples.

Therefore, the question is whether the pores are blocked by Ni particles. Several facts speak against pore blockage: $S(\text{BET})_{\text{mod}}$ and $V_{\text{P,mod}}$ should significantly decrease due to pore blockage, which is only the case for the DI samples. The pore size distributions should also give hints to pore blockage, which is also not observed. In addition, the high dispersions (Fig. 9c) indicate that the Ni particles are accessible. The high extents of reduction (Fig. 9a) also show that most of the Ni is completely oxidized, which means that the Ni is accessible to oxygen. Thus, the pores are obviously not blocked by Ni particles, even though the Ni particle size is similar to the pore size. This can be explained by the fact that the Ni particle size and the pore size are mean values which are determined with different methods. Hence, we can assume that the particle size and the pore size do not exactly coincide. In addition, the $\gamma\text{-Al}_2\text{O}_3$ support does not contain uniform cylindrical pores, but possesses a disordered pore network with a quite broad pore size distribution (Fig. 2) and not a one-dimensional pore system. Even if spherical Ni particles with the same diameter are located in the pores, the irregular geometry of the pore system should still provide enough voids. Hence, the Ni particles should be accessible even if the pore entrances are partially blocked by Ni particles.

For the samples 32DI and 40DI, the Ni surface decreases considerably (Fig. 10). The TPR profiles showed that also with these samples the maximum amount of $\text{T}(\text{Ni}^{2+})/\text{O}(\text{Ni}^{2+})$ species (dispersion capacity) is reached, which means that the $\text{T}(\text{Ni}^{2+})/\text{O}(\text{Ni}^{2+})$ species should also for 32DI and 40DI reach the Ni surface area of the dispersion capacity (Fig. 10, dotted line). Thus, Fig. 12 shows that the Ni particles of the $\text{T}(\text{Ni}^{2+})/\text{O}(\text{Ni}^{2+})$ species generate the main part of the Ni surface. During N_2 physisorption, we assumed that for the 32DI and 40DI samples part of the precursor is located outside the mesopore system on the external surface of the support. During the calcination, these NiO particles cannot be stabilized by the pores so that large NiO particles are formed, which explains the jump of the NiO crystallite size for 32DI (30DI: $\bar{d}_c(\text{NiO}) = 7 \text{ nm}$, 32DI: $\bar{d}_c(\text{NiO}) = 23 \text{ nm}$, Fig. 3). The assumption that the large NiO particles are outside the mesopores is confirmed by the fact that the NiO crystallites are much larger than the maximum of the pore size distribution (Fig. 2). This can also explain the course of the modified pore volume which is related to the support mass

(Fig. 1). For the samples 14DI to 30DI, the pore volume is smaller than the one of the pure support, since the Ni is located in the mesopores, and the difference between the pore volume of the pure support and the samples corresponds roughly to the volume of the metallic Ni. For the samples 32DI and 40DI, the pore volume increases significantly, since only a part of the Ni is in the pores. Hence, the difference between the Ni surface area of the catalyst and the Ni surface area at the dispersion capacity should be caused by the large Ni particles outside the mesopores on the external surface of the support. Thus, with the plot in Fig. 10, we can estimate how large the contribution of the NiO particles to the Ni surface is, and the considerable difference between the Ni surface areas of 30DI and 32DI is caused by the fact that 30DI contains many small NiO particles and 32DI a few large NiO particles (Fig. 11).

During deposition precipitation, Ni is due to the formation of a hydroalumite-like precursor [82] also at high Ni loadings completely deposited in the mesopores. Therefore, the increase of the Ni surface continues even at high Ni loadings, where with dry impregnation lower Ni surface areas are obtained. For the WI samples, N_2 physisorption and TPR show that a significant part of unsupported Ni is present, which is also confirmed by the large NiO crystallite size ($\geq 19 \text{ nm}$, Fig. 3). Since also for the WI samples the maximum amount of $\text{T}(\text{Ni}^{2+})/\text{O}(\text{Ni}^{2+})$ species is formed, the Ni surface area of the dispersion capacity is reached. An increase of the Ni loading leads only to a higher amount of $\text{F}(\text{NiO})$, since the Ni amount in the mesopores is constant. The large NiO particles have a small surface/volume ratio and contribute only to a small extent to the Ni surface, and a small slope is observed with increasing Ni loading (Fig. 10). Whereas with the Ni loading of the dispersion capacity ($0.16 \text{ g}(\text{NiO})$ per $100 \text{ m}^2 \gamma\text{-Al}_2\text{O}_3$) a Ni surface area of 8.3 m^2 per $100 \text{ m}^2 \gamma\text{-Al}_2\text{O}_3$ is obtained, a further increase of the Ni loading to a ninefold value leads only to an increase of 7 m^2 per $100 \text{ m}^2 \gamma\text{-Al}_2\text{O}_3$. This also shows that the Ni is less effectively used as soon as the Ni precursor is located outside the mesopores.

These considerations are also important for the particle size distribution. If Ni is not completely located in the mesopores, the large Ni particles outside the mesopores on the external surface of the support should lead to a bimodal particle size distribution. Since the Ni particle size in the mesopores is determined by the mesopore diameter, this Ni particle size is independent of the Ni loading. The size of the particles outside the mesopores increases with increasing Ni loading, which means that small Ni particles with constant size coexist with larger Ni particles with a variable size. Since the $\text{T}(\text{Ni}^{2+})/\text{O}(\text{Ni}^{2+})$ species in surface/interface layers do not lead to visible XRD peaks, the NiO reflections are only affected by Ni present as NiO species ($\text{F}(\text{NiO})$, $\text{B}(\text{NiO})$). Hence, the mean NiO crystallite size of the calcined samples determined by XRD allows for an estimation of the crystallite size outside the mesopores (Fig. 12a)). For the samples with NiO species in the mesopores (14DI to 30DI, 18DP to 36DP), the NiO crystallite size is small and coincides with the Ni crystallite size (Fig. 3). Most of the NiO in the samples 32DI, 40DI and 30WI to 88WI is outside the mesopores, and, thus, the NiO crystallite size is mainly determined by these large NiO particles. This explains the jump of the NiO crystallite size to higher

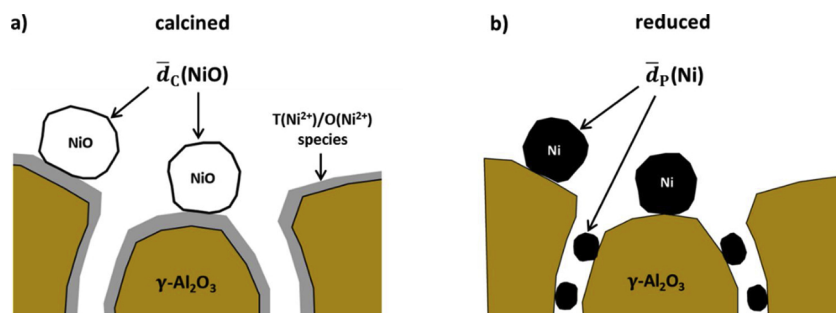


Fig. 12. a) Mean NiO crystallite size $\bar{d}_c(\text{NiO})$ of the calcined samples determined with XRD and b) mean Ni particle size $\bar{d}_p(\text{Ni})$ of the reduced samples determined with H_2 chemisorption.

values compared to the samples with NiO inside the mesopores (14DI to 30DI, 18DP to 36DP). During the reduction, small Ni particles are formed from the $T(Ni^{2+})/O(Ni^{2+})$ species in the mesopores, and large Ni particles (which can consist of several crystallites) result from the reduction of the large NiO particles outside the mesopores (Fig. 12b)).

3.7. Catalytic investigation of the activity

First of all, the activation energies of the samples were determined (see supplementary data for details, Fig. S7). There was no significant dependence on the Ni loading or the preparation method, and all catalysts had similar values between 79 and 86 kJ mol^{-1} . In the literature, activation energies on Ni catalysts between 54 and 106 kJ mol^{-1} are reported [86]. Weatherbee and Bartholomew [86] point out that the low activation energies are due to mass transport limitations. Furthermore, they show that in different meaningful studies values between 80 and 86 kJ mol^{-1} are obtained, which is in perfect agreement with the values of this study.

Afterwards, microscopic influences on the catalytic activity were investigated. The most fundamental parameter of the activity is the number of converted molecules per active site per time unit, i.e., the turnover frequency (TOF) [69]. For the determination of the TOF, a relatively moderate reaction temperature of 300 °C was chosen for a duration of 6 h. The deactivation of the catalysts under these conditions was studied with the time on stream behavior and return point 1 (see supplementary data for details, Fig. S7), and only catalyst 51CP deactivates significantly (for 51CP: $\Delta\bar{X}(\text{CO}_2)_{\text{RP1}} = -22.4\%$, for all other catalysts: $\Delta\bar{X}(\text{CO}_2)_{\text{RP1}} \leq -3.6\%$, Table S7). Hence, the catalytic results of all other catalysts are not influenced by deactivation.

The nominal TOF values of the different catalysts are plotted in Fig. 13. It is obvious that the nominal TOF does not differ considerably. Therefore, we can assume that the different Ni species formed by the different preparation methods (F(NiO), B(NiO), T(Ni²⁺)/O(Ni²⁺), Ni(Al)O_x), AlO_x particles on the metal surface and metal-support interactions do not have a significant influence on the activity. This is the case even though Ni particles formed from different species should have different metal-support interactions. For example, the Ni particles of 14DI result only from T(Ni²⁺)/O(Ni²⁺) species in Al(Ni)O_x. Thus, these Ni particles should have a close contact to the support, whereby different metal-support interactions are possible (electronic influence, support-induced particle morphology, metal-support interface effects [87]). In the WI catalysts, large unsupported Ni particles are formed (F(NiO)). The Ni particles of the DP and CP catalysts are formed from Ni(Al)O_x species, and it is known that, during the reduction of these

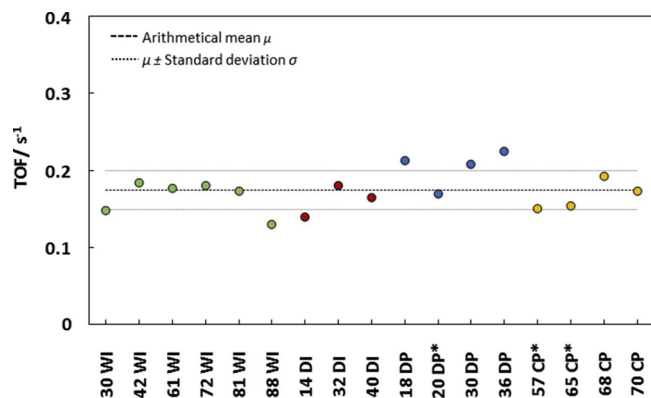


Fig. 13. TOF determined over a period of 6 h at 300 °C, 200 kPa, $X(\text{CO}_2) = 30\%$; mean deviation of the values: factor 1.3 (arithmetical mean $\mu: 0.17 \text{ s}^{-1}$, dashed line); standard deviation $\sigma: 0.025 \text{ s}^{-1}$ (dotted line: $\mu \pm \sigma$); maximum deviation of the values: factor 1.7 (minimum TOF = 0.13 s^{-1} (88WI), maximum TOF = 0.23 s^{-1} (36DP)). The samples with a significant Na mass fraction are marked with an asterisk.

species, AlO_x particles are formed in the Ni particles on the particle surface [55,88]. Ribeiro et al. [69] state in a review on the reproducible measurement of the TOF in metal catalysis that metal-support interactions can change the TOF of the pure metal up to a factor of 100. Bartholomew et al. explain the 10 times larger TOF of a Ni/TiO₂ catalyst as compared to a Ni/SiO₂ catalyst in the CO methanation with different metal-support interactions [89]. In this work, the mean deviation of the TOF values is a factor of 1.3, and the maximum deviation is a factor of 1.7. Hence, all these parameters obviously do not affect the nominal TOF here.

Another possibility is that the catalyst activity is changed by the presence of alkali metal oxides. However, the activity difference of 18DP and 20DP is small, even though the Na mass fraction w_{Na} differs by a factor of 10 (Table S6). For 18DP, 30DP and 36DP, the Na mass fraction is $\leq 0.4\%$. Within these three samples, 36DP with the highest w_{Na} value shows the highest TOF. For 70CP, the Na mass fraction $w_{\text{Na}} = 0.0\%$ (see Table S6), for 68CP, $w_{\text{Na}} = 0.1\%$. However, the TOF on 68CP is slightly higher than the one on 70 CP (Fig. 13). Therefore, at least a significant detrimental influence of Na₂O on the catalyst activity can be excluded.

Furthermore, the particle size can have an important influence on the activity. It is known that in many reactions the activity is significantly dependent on the particle size [90]. For the classification of the structure dependence, Nørskov et al. recently introduced the “degree of structure sensitivity” [91]. For the determination, the converted molecules are normalized per metal surface area and plotted doubly logarithmically against the inverse particle size. Depending on which type of surface atoms (e.g., face, corner, edge atoms) the rate-determining step of the reaction occurs, a different slope α is obtained. By means of the slope α , the active sites can be identified [91] (see Supplementary data for details). The slope α defines the degree of structure sensitivity. In Fig. 14, the slope α is 0.05. This means that the CO₂ methanation is a structure-insensitive reaction, and the terrace atoms can be identified as active sites. Fig. 14 also shows unambiguously that the activity in the particle size range studied would have to change by one or two orders of magnitude, if corner or step atoms were the active sites. This is a strong argument for the fact that the CO₂ methanation on Ni is not affected by geometrical effects. Furthermore, the plot shows that the activity does not depend on metal-support interfaces and metal-support interactions, since these properties change significantly with the particle size. In this work, the TOF is constant, which shows that the activity in the CO₂ methanation is a specific property of the Ni and depends only to a small extent on the preparation method and the Ni loading.

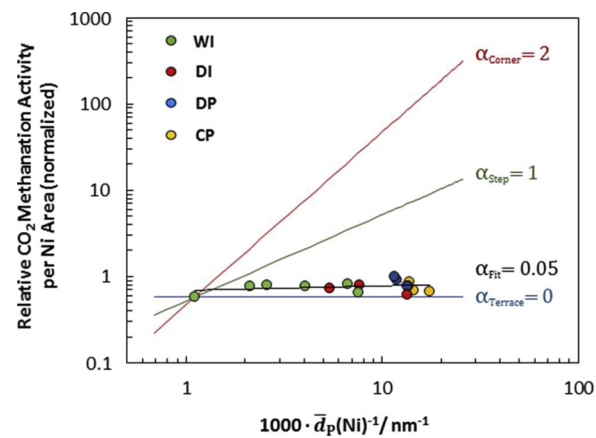


Fig. 14. Determination of the degree of structure sensitivity (α) after Nørskov et al. [91]: Doubly logarithmic plot of the normalized number of converted CO₂ molecules per Ni surface area per time unit versus the inverse mean particle diameter.

Newer investigations with different methods (XPS, HR-TEM) prove that AlO_x particles are formed on the surface of the Ni particles of co-precipitated and impregnated $\text{Ni-Al}_2\text{O}_3$ catalysts [92–94]. Zieliński shows with a thermodynamic consideration that the AlO_x particles should preferably be attached to corner, edge and step atoms [95]. Zank und Zieliński stress that the influence of the AlO_x particles on the catalysis has not been understood yet [96]. Therefore, the question is whether this effect can disguise the particle size dependence. Through a blockage of the corner, edge and step atoms, their number would not be dependent on the particle size any more. However, this is unlikely, since the catalysts have different Ni species: $\text{F}(\text{NiO})$, $\text{B}(\text{NiO})$, $\text{Al}(\text{Ni})\text{O}_x$ species and $\text{Ni}(\text{Al})\text{O}_x$ species with different amounts of Al^{3+} . Thus, the amount of AlO_x particles on the Ni particles should be different. Very similar TOF values for different catalysts in a structure-sensitive reaction due to the AlO_x particles is unlikely, since in this case always the same number of surface atoms with low coordination number would have to be blocked, even though the number of the AlO_x particles on the Ni particles differs strongly. Hence, we can exclude a significant influence of the AlO_x particles on the activity in the CO_2 methanation in this study.

Generally, it is assumed that the CO_2 methanation is a structure-sensitive reaction [28–31]. However, only one of these studies was conducted with an Al_2O_3 support [29], whereas other supports were used in the other reports (ZrO_2 [31], SiO_2 [28,30]). Nonetheless, we observe a distinct structure-insensitive behavior. With 20 different catalysts prepared by 4 different methods with a wide range of Ni loadings (14–88 wt.-%) and mean particle sizes ($\bar{d}_p(\text{Ni}) = 5\text{--}91\text{ nm}$), this study is the most comprehensive study on $\text{Ni-Al}_2\text{O}_3$ catalysts for the CO_2 methanation which is currently available. Hence, the question is why the CO_2 methanation is generally assumed to be a structure-sensitive reaction. Presumably, this claim is based on the assumption that the CO_2 methanation shows the same structure dependence as the CO methanation. The fact that the CO methanation is a structure-sensitive reaction has achieved wide acceptance within the last 20 years due to theoretical investigations. Before 2000, it was mostly assumed that the CO methanation on Ni is a structure-insensitive reaction [69]. Today, it is assumed that the activity for the CO methanation is significantly dependent on the structure and that the corner and step atoms are the active sites of supported catalysts [91].

The theoretical investigations consistently point to a structure dependence of the CO methanation, whereas the experimental studies present contradictory results. The majority of experimental investigations assume that the CO methanation is a structure-insensitive reaction. In surface science studies on well-defined Ni single crystal surfaces, the CO methanation shows a structure-insensitive behavior: The TOF on the open $\text{Ni}(100)$ surface is similar to the one on the closely packed $\text{Ni}(111)$ surface [97–99]. Also well-defined model catalysts demonstrate structure insensitivity: The TOF does not change with an increase of the Ni particle diameter on a SiO_2 film [100] and an Al_2O_3

film [101]. Ribeiro et al. [69] report on many studies where the CO methanation on Ni/SiO_2 and $\text{Ni/Al}_2\text{O}_3$ catalysts is structure-insensitive. By contrast, Bartholomew et al. [102] discuss different studies in which a structure-sensitive behavior of the CO methanation is observed. They explain the different TOF values of these investigations by different extents of reduction and metal-support interactions and stress that the deviations are probably not due to different particle sizes [102]. Nørskov et al. [91,103] determined on a supported Ni catalyst a degree of structure sensitivity of $\alpha = 1.6$ (22 wt.-% Ni; MCR2X catalyst from HaldorTopsøe). The degree of structure sensitivity indicates that the corner and step atoms are the active sites.

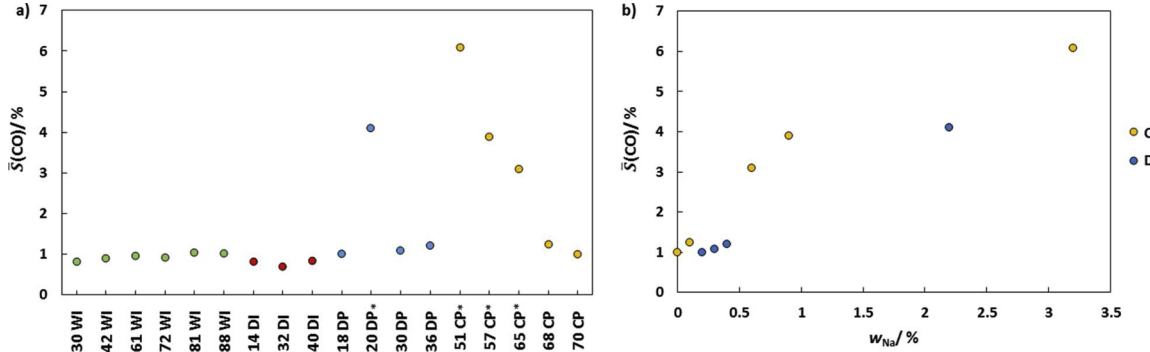
Thus, the question is why so many convincing theoretical studies do not agree with the experimental studies and which effects could cause the structure-insensitive behavior in the experiments. Metal-support interactions cannot be responsible, since structure-insensitivity is also observed on well-defined single crystal surfaces. Hirano und Tanaka [104] explain the structure-insensitive behavior of the CO methanation on $\text{Ni}(100)$ and $\text{Ni}(111)$ surfaces with the formation of carbonaceous deposits. Andersson et al. [103] speculate that defect sites on the single crystal surfaces are the actual active sites and explain the structure insensitivity with a constant defect site density on the different single crystal surfaces. However, this does not explain the structure-sensitive behavior on model and supported catalysts. Therefore, this discussion clearly shows that the structure dependence of the CO methanation has not been clarified yet, and this then obviously also holds for the structure dependence of the CO_2 methanation.

Hence, the results of this study are important for the development of industrial catalysts. Since we show that the catalytic activity does not depend on the particle size or other parameters, the microscopic property which determines the conversion is the Ni surface area. For the preparation of catalysts with a maximum weight time yield, the Ni surface area has to be maximized (see Section 3.9).

3.8. Investigation of the selectivity to CO

After having discussed the catalytic activity, we now focus on the selectivity to CO. A meaningful comparison of selectivities is only possible at similar conversions. Since a constant conversion of 30% was set for the determination of the TOF at 300 °C, these results are well suited for a comparison of the selectivities to CO. On most of the catalysts, CO is formed as the only byproduct (selectivities to $\text{C}_2\text{H}_6 \leq 0.2\%$). Exceptions are 20DP ($\bar{S}(\text{C}_2\text{H}_6) = 1.3\%$), 51CP ($\bar{S}(\text{C}_2\text{H}_6) = 3.2\%$), 57CP ($\bar{S}(\text{C}_2\text{H}_6) = 0.7\%$) and 65CP ($\bar{S}(\text{C}_2\text{H}_6) = 0.4\%$)). Fig. 15a) shows that the selectivity to CO is constant for most of the catalysts. Only on 20DP and 51CP to 65CP, higher selectivities to CO are observed.

There is obviously no significant influence of the Ni particle size on the selectivity to CO, since there is no difference in the CO selectivity of the DI and WI samples with negligible Na mass fractions even though



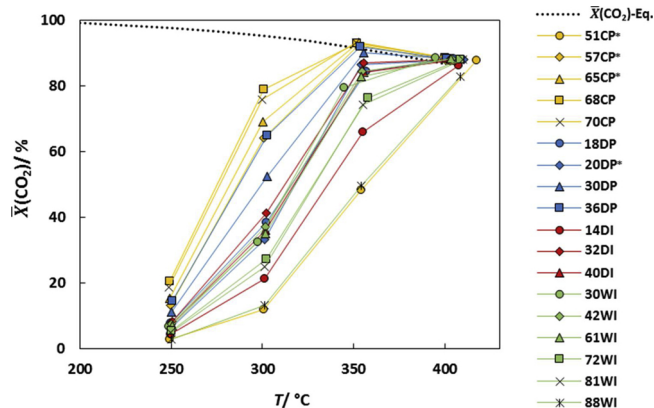


Fig. 16. Mean CO_2 conversions ($\bar{X}(\text{CO}_2)$) determined over a period of 3 h at each temperature at 200 kPa and a modified residence time $\tau_{\text{mod}} = 49.5 \text{ kg s m}^{-3}$. The equilibrium conversion $\bar{X}(\text{CO}_2)\text{-Eq.}$ was calculated with an empirical equilibrium constant from Aparicio [32,113].

the particle size varies between 7 and 91 nm. In addition, $\bar{S}(\text{CO})$ of the catalysts 51CP to 65CP are quite different, even though the Ni particle size is nearly the same (Fig. 9d). $\bar{S}(\text{CO})$ of 20DP also differs clearly from $\bar{S}(\text{CO})$ of the other DP catalysts, even though all DP samples have a comparable Ni particle size. It is noticeable that only on the catalysts with a significant Na mass fraction a higher selectivity to CO is obtained. In Fig. 15b), $\bar{S}(\text{CO})$ is plotted versus the Na mass fraction, and it is obvious that the selectivity to CO correlates with w_{Na} .

To the best of our knowledge, this is the first time that the influence of the Na content on the selectivity in the CO_2 methanation is recognized. In the CO methanation, the influence of Na on the selectivity has been identified and explained in a few investigations [105,106]. The influence of alkali metals on the CO methanation has been discussed [107]. Na contents $\geq 0.5 \text{ wt.-%}$ lead to a decreased activity and to higher selectivities to hydrocarbons (C_xH_y , $x > 1$) [105,106]. The question is now why higher Na mass fractions lead to a higher selectivity to CO. In the reaction mechanism of the CO_2 methanation, it is assumed that CO_2 is converted to CO and that afterwards CO is hydrogenated to CH_4 with the same reaction mechanism as in the CO methanation. Due to the nearly constant TOF, Na seems to have no influence on the CO_2 conversion (Section 3.7.). Hence, a higher selectivity to CO is obtained, since Na_2O might suppress the further conversion of CO to CH_4 .

Because of the lacking investigations on the physicochemical interaction between Na_2O and Ni surfaces, we focus on studies with K_2O , and we can assume that K_2O and Na_2O have similar effects. Zank and Zielinski show in a TPD/TPSR investigation that K_2O on a $\text{Ni}/\text{Al}_2\text{O}_3$ catalyst leads to a stronger CO adsorption [93]. In addition, they observe a more difficult hydrogenation of the adsorbed CO and the adsorbed C. This effect is not explained by Zank and Zielinski, but can be understood with other studies: It can be shown with XPS, that K_2O increases via a Ni-O-K species the electron density on the Ni surface [108], which should lead to a higher binding energy of CO_{ads} and C_{ads} [109], and this can explain the more difficult hydrogenation of adsorbed C. Due to the higher electron transfer from the Ni surface to the $\pi^* - \text{CO}$ antibonding orbital, Na_2O and K_2O should lead to a weakening of the C-O bond. And as a matter of fact, the promotion of Ni surfaces with K facilitates the dissociation of CO [93]. According to the classical mechanism of the CO methanation, the direct dissociation of CO is the rate-determining step [110,111]. Hence, it is difficult to understand that the CO methanation is suppressed by Na_2O . The more difficult hydrogenation of CO in the presence of K_2O and the suppression of the CO methanation by an increase of the Na mass fraction, hence, contradict the classical mechanism. This contradiction can be understood with new theoretical studies which show that the activation energy of the direct CO dissociation is significantly higher than the activation

energy of the CO desorption [103]. Therefore, it is assumed that the CO bond scission proceeds via a COH intermediate (H-assisted dissociation). Surface science studies show that the dissociative adsorption of hydrogen on $\text{Ni}(100)$ and $\text{Ni}(111)$ surfaces decreases through K and that the H coverage is significantly decreased [112]. Andersson et al. show with a DFT calculation that the COH reaction path is suppressed with increasing H coverage [103]. Hence, Na_2O leads to a lower H coverage and, in this way, suppresses the CO methanation.

However, this does not explain why Na_2O suppresses the CO conversion, but does not have an influence on the CO_2 conversion. Generally, it is accepted that the OC–O bond scission is not limited and occurs already at lower temperatures than the C–O bond scission [110]. Zank and Zielinski [93] observe that it is easier to hydrogenate O_{ads} than CO_{ads} or C_{ads} and that K_2O has no influence on the hydrogenation of O_{ads} . Hence, the lower H coverage due to Na_2O has no influence on the CO_2 conversion, since the OC–O bond scission is not limited and the O_{ads} formed is the species which is most easily hydrogenated.

In conclusion, the higher selectivity to CO through the higher Na mass fraction can be explained as follows: Na_2O decreases the H coverage. This has no significant influence on the CO_2 conversion, which is why the same amount of CO molecules is formed on the Ni surface. Through the lower H coverage, less CO is converted via H-assisted CO dissociation. The unconverted CO molecules desorb and thereby increase the selectivity to CO.

3.9. Catalytic investigations at constant modified residence time

After studying the catalytic properties on the microscopic level, we continue on the macroscopic level and determine the conversions on the different catalysts at a constant modified residence time. The mean conversions of the WI and DI catalysts followed the following trend: $\bar{X}(\text{CO}_2)$: 14DI < 40DI < 32DI; $\bar{X}(\text{CO}_2)$: 88WI < 81WI < 72WI < 30WI \approx 42WI \approx 61WI (Fig. 16). This can be understood with the insight from the catalytic investigation on the microscopic level: Since the same amount of CO_2 molecules is converted on the active sites, the different conversions should be due to the different numbers of active sites per catalyst mass. Since the terrace sites were identified as active sites and since their number is proportional to the Ni surface of the catalyst, the mean conversion follows the trend of the Ni surface area.

Obviously, the conversions at 350 and 400 °C are slightly higher than the equilibrium conversions calculated. This can be due to small experimental errors (e.g., deviation of the adjusted $n_{\text{H}_2}/n_{\text{CO}_2}$ ratio) or a small error of the calculation, since an empirical equilibrium constant was applied [113]. The equilibrium conversions reported in the literature calculated with thermodynamic simulations also differ slightly [114].

The largest mean conversions were obtained on the coprecipitated catalysts with the largest Ni surface areas (65CP to 70CP). Also with the CP samples, the mean conversion increases with increasing Ni surface area: $\bar{X}(\text{CO}_2)$: 51CP < 57CP < 65CP < 70CP \approx 68CP. The same holds for the catalysts prepared by deposition precipitation: $\bar{X}(\text{CO}_2)$: 18DP \approx 20DP < 30DP < 36DP. Thus, for all catalysts prepared by the same method, the mean conversion increases with increasing Ni surface area.

To further demonstrate this dependence, the mean conversions at 300 °C are plotted versus the Ni surface areas (Fig. 17). At 250 °C, the same behavior can be observed. There is a linear correlation between the mean conversion and the Ni surface area, which confirms that the mean conversion mainly depends on the number of active sites per catalyst mass. The correlation is better if only the supported catalysts are regarded ($R^2_{300^\circ\text{C}} = 0.95$; $R^2_{250^\circ\text{C}} = 0.95$), and slightly worse if also the coprecipitated catalysts are included in the calculation ($R^2_{300^\circ\text{C}} = 0.89$; $R^2_{250^\circ\text{C}} = 0.90$). The most conspicuous deviation is the fact that on 36DP and 57CP the conversions are similar, even though the Ni surface area of 36DP is much smaller ($\Delta S(\text{Ni}) = 42\%$). The reason for this is that on 36DP the highest TOF value of this work is

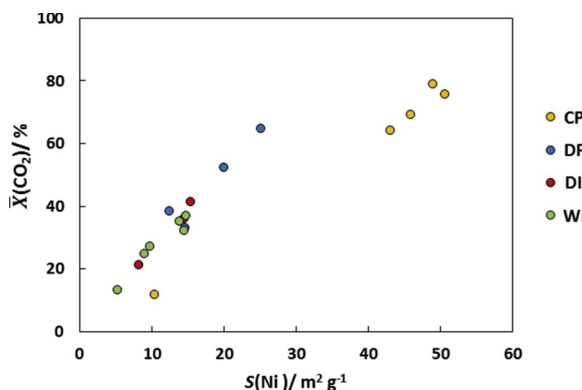


Fig. 17. Mean conversion ($\bar{X}(\text{CO}_2)$) at 300 °C in dependence of the Ni surface area ($S(\text{Ni})$). Linear regression of the supported catalysts: $R^2_{300^\circ\text{C}} = 0.95$; linear regression of all catalysts: $R^2_{300^\circ\text{C}} = 0.89$ (51CP was not included because of the unstable conversion, see Section 3.10).

achieved, whereas on 57CP, one of the lowest TOF values was measured ($\Delta\text{TOF} = 33\%$, factor 1.5). The relative deviation of the Ni surface area corresponds approximately to the relative TOF deviation ($\Delta S(\text{Ni}) = 42\%$, $\Delta\text{TOF} = 33\%$).

Hence, we can conclude that there is a linear correlation between the mean conversion and the Ni surface area. Another important conclusion is that small differences on the microscopic level (TOF) lead due to the high number of active sites to non-negligible differences on the macroscopic level ($\bar{X}(\text{CO}_2)$). The differences increase with increasing Ni surface areas.

In Fig. 18, the mean conversions at 300 °C are plotted versus the Ni mass fractions which represents how effectively the Ni is used in the different catalysts. For the impregnated catalysts, an increase of the Ni loading does not result in a higher conversion, since the Ni dispersion decreases considerably with increasing Ni loading. For the WI catalysts, the conversion stays more or less constant and decreases at Ni mass fractions over 61%. For the DP and CP catalysts, the Ni dispersion stays nearly constant at higher Ni loadings. Therefore, an increase of the Ni mass fraction is an appropriate method to increase the conversion of the catalysts prepared by precipitation.

Besides the conversion, the selectivity is an important parameter for the evaluation of catalysts for an industrial application. Since CO is the only byproduct obtained in considerable amounts, the selectivities to CO are compared in Fig. 19. For the catalysts with significant Na mass fractions, higher selectivities to CO are observed. The selectivities to CO follow the trend of the Na mass fraction ($\bar{S}(\text{CO})$): 51CP > 20DP > 57 CP > 65CP. With increasing conversion, the selectivities to CO decrease considerably for these samples. However, since the conversions are different in Fig. 19, Fig. 15 in Section 3.8. is more appropriate for a meaningful comparison of the selectivities. For the samples with low Na

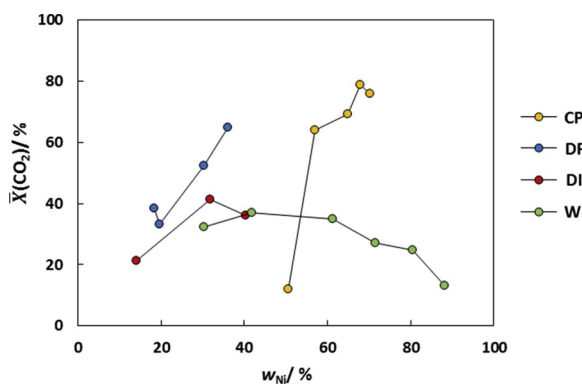


Fig. 18. Mean conversions ($\bar{X}(\text{CO}_2)$) at 300 °C in dependence of the Ni mass fraction.

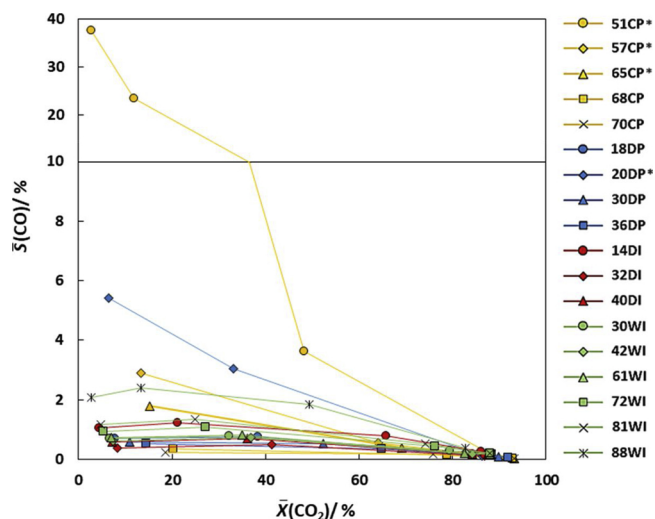


Fig. 19. Mean selectivities to CO ($\bar{S}(\text{CO})$) in dependence of the mean conversion ($\bar{X}(\text{CO}_2)$) at 200 kPa and a modified residence time $\tau_{\text{mod}} = 49.5 \text{ kg s m}^{-3}$. The catalysts with a significant Na mass fraction are marked with an asterisk.

mass fractions, small selectivities to CO are observed. An exception is 88WI with a higher selectivity to CO in spite of a low Na mass fraction. This could be explained with the considerably lower conversion of 88WI compared to the other catalysts with low Na mass fractions.

In the previous paragraphs, we showed that the conversions are largely different, whereas the selectivities of the samples without significant Na mass fractions are nearly constant. Therefore, differences in the weight time yields should mainly be due to the different conversions. Since there is a linear correlation between the conversion and the Ni surface area, the differences in the weight time yields agree well with the trend of the Ni surface area (Fig. 20). For a maximal weight time yield, the Ni surface area of the catalysts has to be maximized.

The small difference in the weight time yield of catalysts 36DP and 65CP is due to the TOF difference which was already discussed above. The weight time yield on 57CP is at 250 °C even smaller than the one of 36DP, since in addition to the lower TOF a higher selectivity to CO is observed due to the higher Na mass fraction. At 300 °C, the selectivity to CO on 57CP is smaller, for which reason also the weight time yield difference to 36DP decreases. At 250 °C, there is a considerable difference between the weight time yields of 36DP and 68CP. At 300 °C, the difference is much smaller, presumably because the conversion on 68CP is closer to the equilibrium conversion. The closer the conversion is to the equilibrium conversion, the smaller is the reaction rate [32].

An important aim of catalyst development is the maximization of the weight time yield. For a smaller reactor size at constant production capacity, the space time yield is decisive. For industrial applications, catalysts with high space time yields are beneficial, since smaller reactors are usually cheaper [115]. For an economic assessment of the catalysts, we, hence, determined the bulk densities of the best supported catalyst (36DP) and the best coprecipitated catalyst (68CP). The bulk density of 68CP ($\rho \approx 1.4 \text{ g cm}^{-3}$) is considerably higher than the one of 36DP ($\rho \approx 0.8 \text{ g cm}^{-3}$), which leads to larger differences in the space time yields ($\text{STY}(68\text{CP}, 300^\circ\text{C}) = 8 \text{ kg h}^{-1} \text{ dm}^{-3}$; $\text{STY}(36\text{DP}, 300^\circ\text{C}) = 4 \text{ kg h}^{-1} \text{ dm}^{-3}$) than in the weight time yields. Hence, for a set production capacity, a smaller reactor is possible for the coprecipitated catalyst, and 68CP is significantly superior to 36DP for an industrial application.

3.10. Catalyst stability

The deactivation of the catalysts was studied with return point 2 at 300 °C after measuring the conversions at 350 and 400 °C (Fig. S7). The relative conversion changes ($\Delta\bar{X}(\text{CO}_2)_{\text{RP2}} = \frac{\bar{X}(\text{CO}_2) : \text{RP2} - \bar{X}(\text{CO}_2) : 300^\circ\text{C}}{\bar{X}(\text{CO}_2) : 300^\circ\text{C}}$)

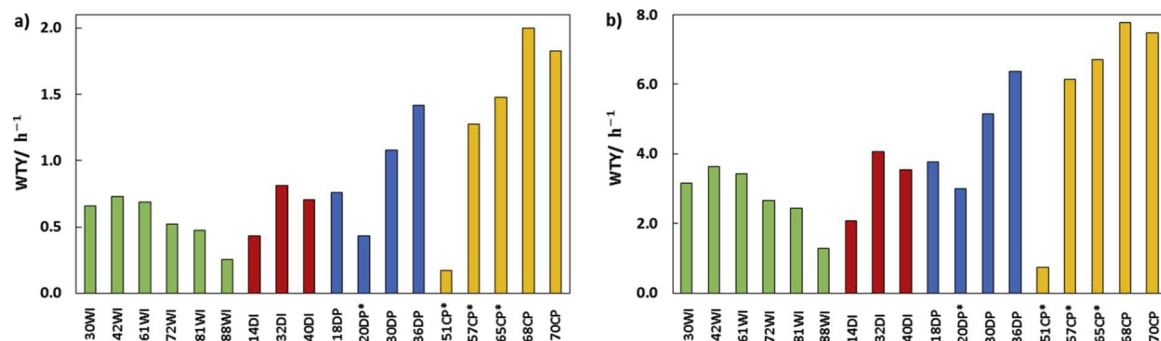


Fig. 20. Weight time yields WTY at 200 kPa and $\tau_{\text{mod}} = 49.5 \text{ kg s m}^{-3}$ and a) 250 °C, b) 300 °C. The catalysts with a significant Na mass fraction are marked with an asterisk.

Table 1

Relative changes after conversion at 350 and 400 °C over a period of 6 h at return point 2 ($\Delta\bar{X}(\text{CO}_2)_{\text{RP2}}$) at 300 °C, 200 kPa and a modified residence time $\tau_{\text{mod}} = 49.5 \text{ kg s m}^{-3}$. Details on the calculation of $\Delta\bar{X}(\text{CO}_2)_{\text{RP2}}$ are given in Eq. (4) of the supplementary data.

Catalyst	$\Delta\bar{X}(\text{CO}_2)_{\text{RP2}}/ \%$
30WI	-12.9
42WI	-12.7
61WI	-15.7
72WI	-15.5
81WI	-17.1
88WI	-14.4
14DI	-11.5
32DI	-12.9
40DI	-12.1
18DP	-11.4
20DP*	-0.5
20DP ^a	0.8
30DP	-9.8
36DP	-8.9
51CP*	104.6
57CP*	13.2
65CP*	4.3
68CP	-6.7
70CP	-13.3

* Samples with significant Na mass fractions.

^a Second experiment.

are listed in **Table 1**. The results in **Table 1** are not meant to compare the stability of the different catalysts, but only to check whether deactivation has an influence on the catalytic results. It would be incorrect to compare catalyst stabilities on the basis of the values in **Table 1**, since the deactivation severities are different (different conversions and, hence, different partial pressures of H₂O). Only together with the results of Table S7 and the study on the change of the metal surfaces under identical conditions in a flow of H₂/H₂O (see below), an assessment of the catalyst stability is possible.

If we assume that the relative conversion changes have an error of $\pm 5\%$, we can state that the supported catalysts show a significant deactivation. 20DP is an exception and does not deactivate. For the CP catalysts 51CP to 65CP, the conversions increase to a smaller extent with increasing $n_{\text{Ni}}/n_{\text{Al}}$. Catalysts 68CP and 70CP deactivate. Therefore, it is important to elucidate the reasons for the deactivation. In addition, we have to solve the question why 20DP does not deactivate and why the deactivation behavior of the CP catalysts changes with $n_{\text{Ni}}/n_{\text{Al}}$.

It is known that carbonaceous deposits can lead to deactivation during CO methanation. During CO₂ methanation, carbonaceous deposits occur to a lesser extent [116]. Thus, we assume that the decrease of the Ni surface area due to sintering is the most likely cause for the

deactivation. The mobility of the Ni particles depends on many parameters (temperature, atmosphere, particle size, metal-support interaction, support texture and impurities [117–119]). In the present study, sintering is favored by the small Ni particle size (< 20 nm; except for 61WI to 88WI) and the steam formed. Since the highest reaction temperature is 400 °C, the deactivation should mainly occur at 400 °C, also because there a large amounts of steam formed at 400 °C due to the high conversions. This assumption is supported by the behavior observed during the determination of the TOF: Over a period of 6 h at 30% conversion and 300 °C, no deactivation is observed (Section 3.7, Table S7).

Interestingly, the catalyst 20DP does not deactivate. The difference to the other supported catalysts is the significant Na mass fraction of 20DP. The Na should occur as Na₂O on the support and/or the Ni surface. Liu et al. [120] point out that an additional oxide phase on the support between or on the metal particles can act as a physical barrier, which can hinder sintering. In addition to the sintering of the metal particles, also the sintering of the γ -Al₂O₃ support has to be considered [121,122]. It is known that the presence of alkali metal and alkaline-earth metal oxides leads to an increase of the thermal stability of γ -Al₂O₃ [122,123]. Hence, the fact that 20DP does not deactivate can be explained with a higher stability of the Ni particles and/or the γ -Al₂O₃ support.

Another interesting fact is that the coprecipitated catalysts 51CP and 57CP ($n_{\text{Ni}}/n_{\text{Al}} = 1$ and 2) show a significant increase of the conversion at return point 2. These catalysts have extents of reduction of only 18% and 67% (Fig. 9a)). Since the CP samples were only activated within 1 h at 500 °C, the extent of reduction could increase during the catalytic investigation. Thus, at return point 2 the Ni surface should be higher due to the higher extent of reduction, which in turn leads to a higher conversion. This assumption was verified by thermogravimetry: After reduction at 400 °C for 3 h, the extent of reduction of 51CP has increased to 28%. Since it is only 5 vol.-% H₂ during thermogravimetry and 80 vol.-% during the reaction, the increase of the extent of reduction should be considerably higher during the reaction. The conversion increase at return point 2 is much higher for 51CP than for 57CP, since the extent of reduction is much lower for 51CP and, as a result of this, the increase of the Ni surface area during the reaction is much higher. We can assume that on all CP catalysts also sintering of the Ni particles occurs which is superimposed with the formation of new Ni particles through an increase of the extent of reduction. Therefore, we can now understand why the increase of the conversion at return point 2 decreases with increasing $n_{\text{Ni}}/n_{\text{Al}}$ and that at $n_{\text{Ni}}/n_{\text{Al}} > 3$, a deactivation is observed: The extent of reduction increases with increasing $n_{\text{Ni}}/n_{\text{Al}}$, and the loss of Ni surface cannot be compensated by the formation of new Ni particles any more. In addition, sintering should be more pronounced at higher $n_{\text{Ni}}/n_{\text{Al}}$.

For a more detailed investigation of the thermal stability, selected samples were aged for 6 h at 600 °C in 15 vol.-% H₂O in H₂. For the discussion, we have to keep in mind that the catalysts have different Ni

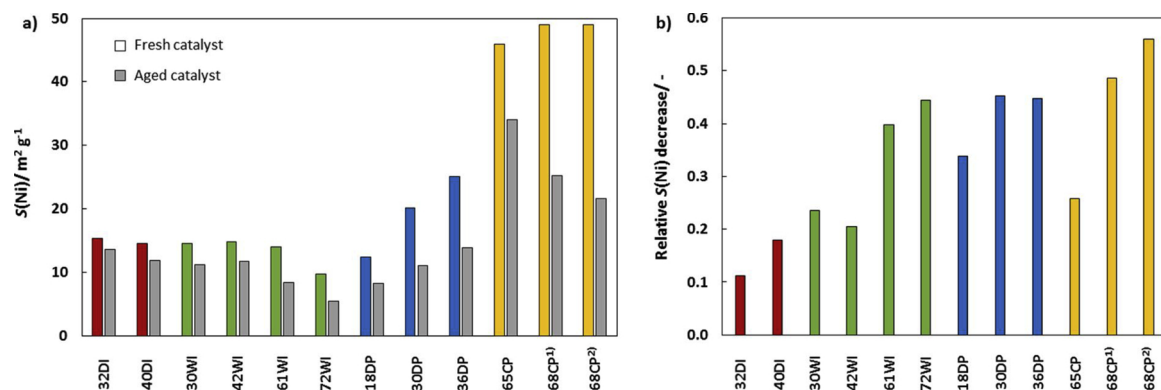


Fig. 21. a) Ni surface area $S(Ni)$ of selected catalysts before and after ageing ($T = 600^\circ C$, $t = 6$ h in 15 vol.-% H_2O in H_2); b) relative decrease of the Ni surface area. ¹⁾ and ²⁾ denote the first and a second reproduction measurement with 68CP.

particle sizes, different Ni loadings and different spatial distributions of the Ni particles. The Ni surface areas before and after ageing are shown in Fig. 21a). For a better comparison of the degree of sintering, Fig. 21b) displays the relative decrease of the Ni surface area.

Catalysts 32DI and 40DI show a small decrease of $S(Ni)$. The relative decrease of $S(Ni)$ for 30WI and 42WI is comparable to the one of 40DI. For 61WI, the relative decrease of $S(Ni)$ is significantly higher than for 42WI, since the amount of Ni in the pores is constant and the additional Ni precipitates in the solution. These unsupported Ni particles have a lower thermal stability. Through the pronounced sintering of these Ni particles, the relative decrease of $S(Ni)$ increases with increasing Ni loading. In the same way as the Ni surface area decreases due to ageing, the mean Ni particle size increases (Fig. S8).

An unexpected result is that $S(Ni)$ of the DP catalysts decreases considerably. Even though the samples 30DP and 36DP have a Ni loading similar to the impregnated samples (32DI, 40DI, 30WI and 42WI), the relative decrease of $S(Ni)$ is nearly twice as large. This shows that the dispersion and the spatial distribution of Ni have a more important influence than the Ni loading. However, it is astonishing that the samples with a higher dispersion have a lower thermal stability, since it is usually assumed that small metal particles have a stronger interaction with the support and that a fine distribution on the support leads to a higher stability [35,37,124]. The relative decrease of $S(Ni)$ for the DP samples is even comparable to the one with the highly loaded WI samples, where also unsupported Ni particles precipitate in the solution. A possible explanation is that there is only a weak interaction between the Ni particles and the support and that the small Ni particles of the DP samples are clearly more mobile than the ones of 32DI, 40DI, 30WI and 42WI. However, during the characterization of the samples, we assumed that the Ni particles are stabilized by the pore walls of the mesopores as soon as the Ni particle size corresponds with the pore diameter. Hence, a higher mobility of the Ni particles should not lead to an increase of the Ni particle size. However, we have to assume that the γ - Al_2O_3 particles sinter and that this leads to a change of the support texture. Therefore, we aged the pure support. Table 2 shows that the BET surface area decreases considerably, whereas the pore volume

stays constant. This behavior is typical for the sintering of γ - Al_2O_3 [125]. The ageing leads to an increase of the pore diameter. Through the smaller surface/volume ratio of the larger pores, a smaller BET surface area is possible at constant pore volume.

Thus, the investigation of the stability of γ - Al_2O_3 shows an increase of the pore diameter. The maximum of the pore size distribution of the aged γ - Al_2O_3 support coincides with the particle size of the aged DP samples (Fig. S8). For 18DP, the relative decrease of $S(Ni)$ is somewhat smaller than for 30DP and 36DP. This can be explained with the fact that the particle size increases more slowly than the pore diameter, since the particle density of 18DP is due to the small Ni loading relatively small.

Hence, the stability of the supported catalysts depends on the spatial Ni distribution and the stability of the support. At a high dispersion, the Ni particles are mainly located in the mesopores and are stabilized by the pore walls. In this case, the stability depends mainly on the stability of the support. Since γ - Al_2O_3 sinters, the stability is lower at high dispersions. The large Ni particles outside the mesopores on the external surface of the support are less prone to sintering, since large Ni particles have a lower mobility. The catalysts with unsupported Ni also have a lower stability, since Ni particles without contact to the support sinter more significantly.

In the coprecipitated samples, the Ni particles are not located separate from each other on a support surface. Nevertheless, the relative decrease of $S(Ni)$ for 65CP is comparable to the one of the supported catalysts 30WI and 42WI with much lower Ni loading. The relative decrease of $S(Ni)$ of 65CP ($n_{Ni}/n_{Al} = 3$) is only about half of the value of 68CP ($n_{Ni}/n_{Al} = 4$). Therefore, $S(Ni)$ of 65CP is after ageing considerably larger than for 68CP, even though $S(Ni)$ of fresh 65CP is lower than the one of fresh 68CP (Fig. 21). In the literature, the thermal stability of coprecipitated catalysts is explained by the fact that during the reduction of the $Ni(Al)O_x$ species AlO_x species form on the particle surface, which separate the Ni particles from each other and protect them against sintering. This “coating” of Ni particles with AlO_x species has been observed directly a number of times [71,92–94]. Our characterization of the coprecipitated samples has shown that the Al^{3+} share of the $Ni(Al)O_x$ species decreases with decreasing n_{Ni}/n_{Al} , which leads to a smaller number of AlO_x species on the Ni particles. Hence, we can expect that the coprecipitated samples with a smaller n_{Ni}/n_{Al} have a higher thermal stability.

A comparison of the selected catalysts shows that 65CP has the highest $S(Ni)$ after ageing. The relative decrease of $S(Ni)$ of 65CP is comparable to the values of the supported catalysts 40DI, 30WI and 42WI. This is remarkable since 65CP has a nearly doubled Ni loading, considerably smaller Ni particles and a nearly threefold fresh $S(Ni)$, which favors sintering. Thus, the coating of the Ni particles with a sufficient number of AlO_x particles can stabilize the Ni particles more effectively than a distribution over the support surface.

Table 2

BET surface areas, pore volumes and mean pore diameters of the γ - Al_2O_3 support in the calcined and aged ($T = 600^\circ C$ or $700^\circ C$, $t = 6$ h in 15 vol.-% H_2O in H_2) state.

	$S(BET)/ m^2 g^{-1}$	$V_p/ cm^3 g^{-1}$	\bar{d}_{Pore}/ nm
calcined	225	0.54	8.9 ^a /7.5 ^b
600 °C	163	0.51	13.8 ^a /11.5 ^b
700 °C	135	0.55	18.2 ^a /13.4 ^b

^a BJH method (adsorption branch).

^b BJH method (desorption branch).

4. Summary and conclusions

In this study, Ni-Al₂O₃ catalysts were prepared by four different preparation methods, i.e., dry impregnation, wet impregnation, deposition precipitation and coprecipitation. The effect of the Ni loading on the Ni surface area and the Ni particle size was systematically studied. Through N₂ physisorption and TPR, the spatial Ni distribution could be elucidated. During deposition precipitation, Ni is via the formation of a hydrotalcite-like precursor completely deposited in the mesopores of the support. During dry and wet impregnation, Ni is partially unsupported or located outside the mesopores on the external surface of the support. If the Ni is in the mesopores, the Ni particle size is independent of the Ni loading and similar to the pore size even at high Ni loadings. Thus, an increase in the Ni loading only leads to a significant increase of the Ni surface area, if the Ni is deposited in the mesopores of the support during the preparation of the catalyst. The Ni particle size of the coprecipitated catalysts is independent of the Ni loading, and thus, an increase of the Ni loading leads to a considerable increase of the Ni surface area in this case. Therefore, deposition precipitation and coprecipitation are the best methods for the preparation of catalysts with high Ni surface areas.

The catalytic investigation clearly shows that the CO₂ methanation on Ni-Al₂O₃ catalysts is a structure-insensitive reaction and that the terrace atoms are the active sites. Other parameters, such as metal-support interactions, the metal-support interface, AlO_x particles or alkali metals do not have a significant influence on the activity. Thus, the activity seems to be a specific property of Ni, and the Ni surface area is the microscopic property which determines the CO₂ conversion. In measurements with a constant modified residence time, a linear correlation between the Ni surface area and the conversion can be observed. Therefore, the catalysts with the highest Ni surface areas achieve the highest weight time yields. Furthermore, with increasing Na mass fraction, a linear increase of the selectivity to CO results. All other catalysts with insignificant Na mass fractions show low and similar selectivities to CO. The stability of the supported catalysts depends on the spatial distribution of Ni and the stability of the support. At high dispersions, the Ni particles are mainly located in the mesopores and stabilized by the pore walls. Since the γ-Al₂O₃ support sinters, the stability is lower at high dispersions. The large Ni particles outside the mesopores on the external surface of the support sinter less due to their reduced mobility. The samples with unsupported Ni particles without contact to the support sinter more significantly. The coprecipitated catalyst 65CP ($n_{\text{Ni}}/n_{\text{Al}} = 3$) shows the highest Ni surface area after ageing, which is explained with a coating of the Ni particles with AlO_x particles, which stabilizes the Ni particles more effectively than a distribution over the support surface.

The results of this study can be applied to prepare catalysts with significantly different particle sizes. Hence, it is a good starting point for further investigations on the dependence of the reaction mechanism on the particle size, e.g., with *in situ* IR spectroscopy.

Acknowledgements

The authors thank thyssenkrupp Industrial Solutions AG for financial support and Dr. Steffen Schirrmeister for valuable guidance. Furthermore, we thank Fiona Schneider for help with the preparation of the coprecipitated catalysts. This research did not receive any specific grant from funding agencies in the public or not-for-profit sectors.

Appendix A. Supplementary data

Supplementary material related to this article can be found, in the online version, at doi:<https://doi.org/10.1016/j.apcatb.2018.12.064>.

References

- [1] M. Götz, J. Lefebvre, F. Mörs, A.M. Koch, F. Graf, S. Bajohr, R. Reimert, T. Kolb, Renewable power-to-gas: a technological and economic review, *Renew. Energy* 85 (2016) 1371–1390, <https://doi.org/10.1016/j.renene.2015.07.066>.
- [2] S. Schiebahn, T. Grube, M. Robinius, V. Tietze, B. Kumar, D. Stolten, Power to gas: technological overview, systems analysis and economic assessment for a case study in Germany, *Int. J. Hydrogen Energy* 40 (2015) 4285–4294, <https://doi.org/10.1016/j.ijhydene.2015.01.123>.
- [3] A. Lewandowska-Bernat, U. Desideri, Opportunities of power-to-gas technology in different energy systems architectures, *Appl. Energy* 228 (2018) 57–67, <https://doi.org/10.1016/j.apenergy.2018.06.001>.
- [4] M. Bailera, P. Lisbona, L.M. Romeo, S. Espatolero, Power to gas projects review: lab, pilot and demo plants for storing renewable energy and CO₂, *Renew. Sustain. Energy Rev.* 69 (2017) 292–312, <https://doi.org/10.1016/j.rser.2016.11.130>.
- [5] S. Rönsch, J. Schneider, S. Matthischke, M. Schlüter, M. Götz, J. Lefebvre, P. Prabhakaran, S. Bajohr, Review on methanation – from fundamentals to current projects, *Fuel* 166 (2016) 276–296, <https://doi.org/10.1016/j.fuel.2015.10.111>.
- [6] P. Sabatier, J.B. Senderens, *Hydrogénéation directe des oxydes du carbone en présence de divers métauxdivisés*, *Acad. Sci.* 134 (1902) 514–516.
- [7] G.A. Du, S. Lim, Y.H. Yang, C. Wang, L. Pfefferle, G.L. Haller, Methanation of carbon dioxide on Ni-incorporated MCM-41 catalysts: the influence of catalyst pretreatment and study of steady-state reaction, *J. Catal.* 249 (2007) 370–379, <https://doi.org/10.1016/j.jcat.2007.03.029>.
- [8] G.D. Weatherbee, C.H. Bartolomew, Hydrogenation of CO₂ on group VIII metals: IV. Specific activities and selectivities of silica-supported Co, Fe, and Ru, *J. Catal.* 87 (1984) 352–362, [https://doi.org/10.1016/0021-9517\(84\)90196-9](https://doi.org/10.1016/0021-9517(84)90196-9).
- [9] F. Solymosi, A. Erdöhelyi, Hydrogenation of CO₂ to CH₄ over alumina-supported noble metals, *J. Mol. Catal.* 166 (1980) 471–474, [https://doi.org/10.1016/0304-5102\(80\)80086-1](https://doi.org/10.1016/0304-5102(80)80086-1).
- [10] P. Panagiotopoulou, D. Kondarides, X. Verykios, Selective methanation of CO over supported noble metal catalysts: effects of the nature of the metallic phase on catalytic performance, *Appl. Catal. A Gen.* 344 (2008) 45–54, <https://doi.org/10.1016/j.apcata.2008.03.039>.
- [11] C. de Leitenburg, A. Trovarelli, J. Kašpar, A temperature-programmed and transient kinetic study of CO₂ activation and methanation over CeO₂ supported noble metals, *J. Catal.* 166 (1997) 98–107, <https://doi.org/10.1006/jcat.1997.1498>.
- [12] M.A.A. Aziz, A.A. Jalil, S. Triwahyono, S. Sidiq, Methanation of carbon dioxide on metal-promoted mesostructured silica nanoparticles, *Appl. Catal. A Gen.* 486 (2014) 115–122, <https://doi.org/10.1016/j.apcata.2014.08.022>.
- [13] Z. Kowalczyk, K. Stolecki, W. Radog-Pilecka, E. Miskiewicz, E. Wiczkowska, Z. Karpinski, Supported ruthenium catalysts for selective methanation of carbon oxides at very low CO_x/H₂ ratios, *Appl. Catal. A Gen.* 342 (2008) 35–39, <https://doi.org/10.1016/j.apcata.2007.12.040>.
- [14] C.H. Bartholomew, C.K. Vance, Effects of support on the kinetics of carbon hydrogenation on nickel, *Appl. Catal.* 7 (1983) 78–87, [https://doi.org/10.1016/0021-9517\(85\)90290-8](https://doi.org/10.1016/0021-9517(85)90290-8).
- [15] S. Tada, T. Shimizu, H. Kameyama, T. Haneda, R. Kikuchi, Ni/CeO₂ catalysts with high CO₂ methanation activity and high CH₄ selectivity at low temperatures, *Int. J. Hydrogen Energy* 37 (2012) 5527–5531, <https://doi.org/10.1016/j.ijhydene.2011.12.122>.
- [16] M.A.A. Aziz, A.A. Jalil, S. Triwahyono, R.R. Mukti, Y.H. Taufiq-Yap, M.R. Sazegar, Highly active Ni-promoted mesostructured silica nanoparticles for CO₂ methanation, *Appl. Catal. B* 147 (2014) 359–368, <https://doi.org/10.1016/j.apcatb.2013.09.015>.
- [17] M.C. Bacariza, I. Graça, S.S. Bebiano, J.M. Lopes, C. Henriques, Micro- and mesoporous supports for CO₂ methanation catalysts: a comparison between SBA-15, MCM-41 and USY zeolite, *Chem. Eng. Sci.* 175 (2018) 72–83, <https://doi.org/10.1016/j.ces.2017.09.027>.
- [18] F.W. Chang, M.S. Kuo, M.T. Tsay, M.C. Hsieh, Hydrogenation of CO₂ over nickel catalysts on rice husk ash-alumina prepared by incipient wetness impregnation, *Appl. Catal. A Gen.* 247 (2003) 309–320, [https://doi.org/10.1016/S0926-860X\(03\)00181-9](https://doi.org/10.1016/S0926-860X(03)00181-9).
- [19] H. Takano, N. Shinomiya, K. Izumiya, N. Kumagai, H. Habazaki, K. Hashimoto, CO₂ methanation of Ni catalysts supported on tetragonal ZrO₂ doped with Ca²⁺ and Ni²⁺ ions, *Int. J. Hydrogen Energy* 15 (2014) 8347–8355, <https://doi.org/10.1016/j.ijhydene.2015.04.128>.
- [20] G.A. Mills, F.W. Steffgen, Catalytic Methanation, *Catal. Rev.* 8 (1974) 159–210, <https://doi.org/10.1080/01614947408071860>.
- [21] G.H. Watson, *Methanation Catalysts. Report Number ICTIS/TR 09, International Energy Agency Coal Research, London, England, 1980*, pp. 1–56.
- [22] O.V. Krylov, K.H. Mamedov, Heterogeneous catalytic reactions of carbon dioxide, *Rus. Chem. Rev.* 64 (1995) 877–900, <https://doi.org/10.1070/RC1995v06n09ABEH000182>.
- [23] W. Wang, J. Gong, Methanation of carbon dioxide: an overview, *Front. Chem. Sci. Eng.* 5 (2011) 2–10, <https://doi.org/10.1007/s11705-010-0528-3>.
- [24] J. Gao, Q. Liu, F. Gu, B. Liu, Z. Zhong, F. Su, Recent advances in methanation catalysts for the production of synthetic natural gas, *RSC Adv.* 5 (2015) 22759–22776, <https://doi.org/10.1039/C4RA16114A>.
- [25] M.A.A. Aziz, A.A. Jalil, S. Triwahyono, A. Ahmad, Recent advances in methanation catalysts for the production of synthetic natural gas, *Green Chem.* 17 (2015) 2647–2663, <https://doi.org/10.1039/C4RA16114A>.
- [26] W. Li, H. Wang, X. Jiang, J. Zhu, Z. Liu, X. Guo, C. Song, A short review of recent advances in CO₂ hydrogenation to hydrocarbons over heterogeneous catalysts, *RSC Adv.* 8 (2018) 7651–7669, <https://doi.org/10.1039/C7RA13546G>.

[27] B. Miao, S.S.K. Ma, X. Wang, H. Su, S.H. Chan, Catalysis mechanisms of CO₂ and CO methanation, *Catal. Sci. Technol.* 6 (2016) 4048–4058, <https://doi.org/10.1039/C6CY00478D>.

[28] C. Vogt, E. Groeneveld, G. Kamsma, M. Nachtegaal, L. Lu, C.J. Kiely, P.H. Berben, F. Meirer, B.M. Weckhuysen, Unravelling structure sensitivity in CO₂ hydrogenation over nickel, *Nat. Catal.* 1 (2018) 127–134, <https://doi.org/10.1038/s41929-017-0016-y>.

[29] S. He, C. Li, H. Chen, D. Su, B. Zhang, X. Cao, B. Wang, M. Wei, D.G. Evans, X. Duan, A surface defect-promoted Ni nanocatalyst with simultaneously enhanced activity and stability, *Chem. Mater.* 25 (2013) 1040–1046, <https://doi.org/10.1021/cm303517z>.

[30] H.C. Wu, Y.C. Chang, J.H. Wu, J.H. Lin, I.K. Lin, C.S. Chen, Methanation of CO₂ and reverse water/gas shift reactions on Ni/SiO₂ catalysts: the influence of particle size on selectivity and reaction pathway, *Catal. Sci. Technol.* 5 (2015) 4154–4163, <https://doi.org/10.1039/C5CY00667H>.

[31] J.K. Kesavan, I. Luisetto, S. Tuti, C. Meneghini, G. Lucci, C. Battocchio, S. Mobilio, S. Casciardi, R. Sisto, Nickel supported on YSZ: the effect of Ni particle size on the catalytic activity for CO₂ methanation, *J. CO₂ Util.* 23 (2018) 200–211, <https://doi.org/10.1016/j.jcou.2017.11.015>.

[32] F. Koschany, D. Schlereth, O. Hinrichsen, On the kinetics of the methanation of carbon dioxide on coprecipitated NiAl(O)x, *Appl. Catal. B* 181 (2016) 504–516, <https://doi.org/10.1016/j.apcatb.2015.07.026>.

[33] C. Li, Y.-W. Chen, Temperature-programmed-reduction studies of nickel oxide/alumina catalysts: effects of the preparation method, *Thermochim. Acta* 256 (1995) 457–465, [https://doi.org/10.1016/0040-6031\(94\)02177-P](https://doi.org/10.1016/0040-6031(94)02177-P).

[34] G. Li, L. Hu, J.M. Hill, Comparison of reducibility and stability of alumina-supported Ni catalysts prepared by impregnation and co-precipitation, *Appl. Catal. A: Gen.* 301 (2006) 16–24, <https://doi.org/10.1016/j.apcata.2005.11.013>.

[35] Y. Bang, S. Park, S.J. Han, J. Yoo, J.H. Song, J.H. Choi, K.H. Kang, I.K. Song, Hydrogen production by steam reforming of liquefied natural gas (LNG) over mesoporous Ni/Al₂O₃ catalyst prepared by an EDTA-assisted impregnation method, *Appl. Catal. B* 180 (2016) 179–188, <https://doi.org/10.1016/j.apcatb.2015.06.023>.

[36] M.A. Goula, N.D. Charisiou, K.N. Papageridis, A. Delimitis, E. Pachatouridou, E.F. Iliopoulos, Nickel on alumina catalysts for the production of hydrogen rich mixtures via the biogas dry reforming reaction: influence of the synthesis method, *Int. J. Hydrogen Energy* 40 (2015) 9183–9200, <https://doi.org/10.1016/j.ijhydene.2015.05.129>.

[37] A. Gil, A. Díaz, L.M. Gandía, M. Montes, Influence of the preparation method and the nature of the support on the stability of nickel catalysts, *Appl. Catal. A: Gen.* 109 (1994) 167–179, [https://doi.org/10.1016/0926-860X\(94\)80116-9](https://doi.org/10.1016/0926-860X(94)80116-9).

[38] J. Choi, S. Zhang, J.M. Hill, Reducibility and toluene hydrogenation activity of nickel catalysts supported on γ -Al₂O₃ and κ -Al₂O₃, *Catal. Sci. Technol.* 2 (2012) 179–186, <https://doi.org/10.1039/C1CY00301A>.

[39] K.V.R. Chary, P.V.R. Rao, V.V. Rao, Catalytic functionalities of nickel supported on different polymorphs of alumina, *Catal. Commun.* 9 (2008) 886–893, <https://doi.org/10.1016/j.catcom.2007.09.016>.

[40] R. Molina, G. Poncelet, α -Alumina-supported nickel catalysts prepared from nickel acetylacetone: a TPR study, *J. Catal.* 173 (1998) 257–267, <https://doi.org/10.1006/jcat.1997.1931>.

[41] X. Wang, B.J. Zhao, D.J. Xie, Y. Xie, Monolayer dispersion of MoO₃, NiO and their precursors on γ -Al₂O₃, *Appl. Catal. A: Gen.* 188 (1999) 201–209, [https://doi.org/10.1016/S0926-860X\(99\)00248-3](https://doi.org/10.1016/S0926-860X(99)00248-3).

[42] P. Kim, H. Kim, J.B. Joo, W. Kim, I.K. Song, J. Yi, Effect of nickel precursor on the catalytic performance of Ni/Al₂O₃ catalysts in the hydrodechlorination of 1,1,2-trichloroethane, *J. Mol. Catal. A: Chem.* 256 (2006) 178–183, <https://doi.org/10.1016/j.molcata.2006.04.061>.

[43] C.H. Bartholomew, R.J. Farrauto, Chemistry of nickel-alumina catalysts, *J. Catal.* 45 (1976) 41–53, [https://doi.org/10.1016/0021-9517\(76\)90054-3](https://doi.org/10.1016/0021-9517(76)90054-3).

[44] K.E. Sedor, M.M. Hossain, H.I. de Lasa, Reactivity and stability of Ni/Al₂O₃ oxygen carrier for chemical-looping combustion (CLC), *Chem. Eng. Sci.* 63 (2008) 2994–3007, <https://doi.org/10.1016/j.ces.2008.02.021>.

[45] C. Jia, J. Gao, J. Li, F. Gu, G. Xu, Z. Zhong, S. Su, Nickel catalysts supported on calcium titanate for enhanced CO methanation, *Catal. Sci. Technol.* 3 (2013) 490–499, <https://doi.org/10.1039/C2CY20542D>.

[46] S. Narayanan, K. Uma, Studies of the effect of calcination on the dispersion and reduction of nickel supported on alumina by X-ray photoelectron spectroscopy, X-ray diffraction, chemisorption and catalytic activity, *J. Chem. Soc. Faraday Trans. 1* (81) (1985) 2733–2744, <https://doi.org/10.1039/F19858102733>.

[47] M. Houalla, F. Delannay, I. Matsuura, B. Delmon, Physico-chemical characterisation of impregnated and ion-exchanged silica-supported nickel oxide, *J. Chem. Soc. Faraday Trans. 1* (76) (1980) 2128–2141, <https://doi.org/10.1039/F19807602128>.

[48] B. Delmon, Reactions during catalyst activation, in: G. Ertl, H. Knözinger, F. Schüth, J. Weitkamp (Eds.), *Handbook of Heterogeneous Catalysis*, 2nd edn., Wiley, Weinheim, 2008, pp. 655–676.

[49] J. Gao, C. Jia, J. Li, F. Gu, G. Xu, Z. Zhong, F. Su, Nickel catalysts supported on barium hexaaluminate for enhanced CO methanation, *Ind. Eng. Chem. Res.* 51 (2012) 10345–10353, <https://doi.org/10.1021/ie300566n>.

[50] T. Wang, H. Ma, L. Zeng, D. Li, H. Tian, S. Xiao, J. Gong, Highly loaded Ni-based catalysts for low temperature ethanol steam reforming, *Nanoscale* 8 (2016) 10177–10187, <https://doi.org/10.1039/C6NR02586B>.

[51] G. Wen, Y. Xu, Z. Xu, Z. Tian, Characterization and catalytic properties of the Ni/Al₂O₃ catalysts for aqueous-phase reforming of glucose, *Catal. Lett.* 129 (2009) 250–257, <https://doi.org/10.1007/s10562-008-9810-0>.

[52] B. Lu, K. Kawamoto, Preparation of the highly loaded and well-dispersed NiO/SBA-15 for methanation of producer gas, *Fuel* 103 (2013) 699–704, <https://doi.org/10.1016/j.fuel.2012.09.009>.

[53] S. Hu, M. Xue, H. Chen, Y. Sun, J. Shen, Preparation of highly loaded and active Ni/Al₂O₃ catalysts for the hydrogenation of aromatic rings, *Chin. J. Catal.* 32 (2001) 917–925, [https://doi.org/10.1016/S1872-2067\(10\)60224-0](https://doi.org/10.1016/S1872-2067(10)60224-0).

[54] M.A. Ermakova, D.Y. Ermakov, High-loaded nickel–silica catalysts for hydrogenation, prepared by poly-gel: route, structure and catalytic behavior, *Appl. Catal. A Gen.* 245 (2003) 277–288, [https://doi.org/10.1016/S0926-860X\(02\)00648-8](https://doi.org/10.1016/S0926-860X(02)00648-8).

[55] E.C. Kruissink, L.L. van Reijen, R.H. Ross, Coprecipitated nickel–alumina catalysts for methanation at high temperature. Part 1.—chemical composition and structure of the precipitates, *J. Chem. Soc. Faraday Trans. 1* (77) (1981) 649–663, <https://doi.org/10.1039/F19817700649>.

[56] L.E. Alzamora, R.H. Ross, E.C. Kruissink, L.L. van Reijen, Coprecipitated nickel–alumina catalysts for methanation at high temperature. Part 2.—variation of total and metallic areas as a function of sample composition and method of pre-treatment, *J. Chem. Soc. Faraday Trans. 1* (77) (1981) 665–681, <https://doi.org/10.1039/F19817700665>.

[57] H.G.J. Lansink Rotgerink, H. Bosch, J.G. van Ommen, J.R.H. Ross, The effect of Ni/Al ratio on the properties of coprecipitated nickel-alumina catalysts with high nickel contents, *Appl. Catal. B* 27 (1986) 41–53, [https://doi.org/10.1016/S0169-9534\(00\)81045-3](https://doi.org/10.1016/S0169-9534(00)81045-3).

[58] S. Abelló, C. Berueco, F. Gispert-Guirado, D. Montané, Synthetic natural gas by direct CO₂ hydrogenation on activated takovites: effect of Ni/Al molar ratio, *Catal. Sci. Technol.* 6 (2016) 2305–2317, <https://doi.org/10.1039/C5CY01200G>.

[59] L. Bian, W. Wang, R. Xia, Z. Li, Ni-based catalyst derived from Ni/Al hydrotalcite-like compounds by the urea hydrolysis method for CO methanation, *RSC Adv.* 6 (2016) 677–686, <https://doi.org/10.1039/CSRA19748A>.

[60] S. Abate, K. Barbera, E. Giglio, F. Deorsola, S. Bensaid, S. Perathoner, R. Pirone, G. Centi, Synthesis, characterization, and activity pattern of Ni–Al hydrotalcite catalysts in CO₂ methanation, *Ind. Eng. Chem. Res.* 55 (2016) 8299–8308, <https://doi.org/10.1021/acs.iecr.6b01581>.

[61] M. Gabrovska, R. Edreva-Kardjieva, D. Crișan, P. Tzvetkov, M. Shopska, I. Shtereva, Ni–Al layered double hydroxides as catalyst precursors for CO₂ removal by methanation, *React. Kinet. Mech. Catal.* 105 (2012) 79–99, <https://doi.org/10.1007/s11144-011-0378-0>.

[62] L. He, Y. Huang, A. Wang, X. Chen, J. Delgado, T. Zhang, A noble-metal-free catalyst derived from Ni-Al hydrotalcite for hydrogen generation from N2H4–H2O decomposition, *Angew. Chem. Int. Ed.* 51 (2012) 6191–6194, <https://doi.org/10.1002/anie.201201737>.

[63] G. Bergeret, P. Gallezot, Particle size and dispersion measurements, in: G. Ertl, H. Knözinger, F. Schüth, J. Weitkamp (Eds.), *Handbook of Heterogeneous Catalysis*, 2nd edn., Wiley, Weinheim, 2008, pp. 738–765.

[64] D.M.A. Monti, A. Baiker, Temperature-programmed reduction. Parametric sensitivity and estimation of kinetic parameters, *J. Catal.* 83 (1983) 323–335, [https://doi.org/10.1016/0021-9517\(83\)90058-1](https://doi.org/10.1016/0021-9517(83)90058-1).

[65] P. Malet, A. Caballero, The selection of experimental conditions in temperature-programmed reduction experiments, *J. Chem. Soc. Faraday Trans. 84* (1988) 2369–2375, <https://doi.org/10.1039/F19888402369>.

[66] D.G. Mustard, C.H. Bartholomew, Determination of metal crystallite size and morphology in supported nickel catalysts, *J. Catal.* 67 (1981) 186–206, [https://doi.org/10.1016/0021-9517\(81\)90271-2](https://doi.org/10.1016/0021-9517(81)90271-2).

[67] C.H. Bartholomew, R.B. Pannell, The stoichiometry of hydrogen and carbon monoxide chemisorption on alumina- and silica-supported nickel, *J. Catal.* 65 (1980) 390–401, [https://doi.org/10.1016/0021-9517\(80\)90316-4](https://doi.org/10.1016/0021-9517(80)90316-4).

[68] D. Beierlein, S. Schirrmeyer, Y. Traa, E. Klemm, Experimental approach for identifying hotspots in lab-scale fixed-bed reactors exemplified by the Sabatier reaction, *React. Kinet. Mech. Catal.* 125 (2018) 157–170, <https://doi.org/10.1007/s11144-018-1402-4>.

[69] F.H. Ribeiro, A.E. Schach von Wittenau, C.H. Bartholomew, G.A. Somorjai, Reproducibility of turnover rates in heterogeneous metal catalysis: compilation of data and guidelines for data analysis, *Catal. Rev.-Sci. Eng.* 39 (1997) 49–76, <https://doi.org/10.1080/01614949708006468>.

[70] C.A. Schwengber, F. Alves da Silva, R.A. Schaffner, N.C.R. Fernandes-Machado, R.F. Ferracin, V.R. Bach, H.J. Alves, Methane dry reforming using Ni/Al₂O₃ catalysts: evaluation of the effects of temperature, space velocity and reaction time, *J. Environ. Chem. Eng.* 4 (2016) 3688–3695, <https://doi.org/10.1016/j.jeche.2016.07.001>.

[71] P. Salagere, J.L.G. Fierro, F. Medina, J.E. Sueiras, Characterization of nickel species on several γ -alumina supported nickel samples, *J. Mol. Catal. A: Chem.* 106 (1996) 125–134, [https://doi.org/10.1016/1381-1169\(95\)00256-1](https://doi.org/10.1016/1381-1169(95)00256-1).

[72] M.K. Titulaer, J.B.H. Jansen, J.W. Geus, The quantity of reduced nickel in synthetic takovite: effects of preparation conditions and calcination temperature, *Clays Clay Miner.* 42 (1994) 249–258, <https://doi.org/10.1346/CCMN.1994.0420303>.

[73] M.R. Quddus, M.M. Hossain, H.I. de Lasa, Ni based oxygen carrier over γ -Al₂O₃ for chemical looping combustion: effect of preparation method on metal support interaction, *Catal. Today* 210 (2013) 124–134, <https://doi.org/10.1016/j.cattod.2013.02.005>.

[74] M. Wu, D.M. Hercules, Studies of supported nickel catalysts by x-ray photoelectron and ion scattering spectroscopies, *J. Phys. Chem.* 83 (1979) 2003–2008, <https://doi.org/10.1021/j100478a015>.

[75] Y. Chen, L. Zhang, Surface interaction model of γ -alumina-supported metal oxides, *Catal. Lett.* 12 (1992) 51–62, <https://doi.org/10.1007/BF00767188>.

[76] J. Richardson, M.V. Twigg, Reduction of impregnated NiO/α-Al₂O₃ association of Al³⁺ ions with NiO, *Appl. Catal. A Gen.* 167 (1998) 57–64, [https://doi.org/10.1016/S0926-860X\(97\)00298-6](https://doi.org/10.1016/S0926-860X(97)00298-6).

[77] R. Yang, X. Li, J. Wu, X. Zhang, Z. Zhang, Y. Cheng, J. Guo, Hydrotreating of crude

2-ethylhexanol over Ni/Al₂O₃ catalysts: surface Ni species-catalytic activity correlation, *Appl. Catal. A Gen.* 368 (2009) 105–112, <https://doi.org/10.1016/j.apcata.2009.08.021>.

[78] S.-C. Ho, T.-C. Chou, The role of anion in the preparation of nickel catalyst detected by TPR and FTIR spectra, *Ind. Eng. Chem. Res.* 34 (1995) 2279–2284, <https://doi.org/10.1021/ie00046a009>.

[79] Y.C. Xie, Y.Q. Tang, Spontaneous monolayer dispersion of oxides and salts onto surfaces of supports: applications to heterogeneous catalysis, *Adv. Catal.* 37 (1990) 1–43, [https://doi.org/10.1016/S0360-0564\(08\)60362-4](https://doi.org/10.1016/S0360-0564(08)60362-4).

[80] G.W. Geus, A.J. van Dillen, Preparation of supported catalysts by deposition-precipitation, in: G. Ertl, H. Knözinger, F. Schüth, J. Weitkamp (Eds.), *Handbook of Heterogeneous Catalysis*, 2nd edn., Wiley, Weinheim, 2008, pp. 428–467.

[81] M.V. Twigg, J.T. Richardson, Effects of alumina incorporation in coprecipitated Ni-Al₂O₃ catalysts, *Appl. Catal. A Gen.* 190 (2000) 61–72, [https://doi.org/10.1016/S0926-860X\(99\)00269-0](https://doi.org/10.1016/S0926-860X(99)00269-0).

[82] P.K. De Bokx, W.B. Wassenberg, J.W. Geus, Interaction of nickel ions with a γ-Al₂O₃ support during deposition from aqueous solution, *J. Catal.* 104 (1987) 86–98, [https://doi.org/10.1016/0021-9517\(87\)90339-3](https://doi.org/10.1016/0021-9517(87)90339-3).

[83] F. Schüth, M. Hesse, K.K. Unger, Precipitation and coprecipitation, in: G. Ertl, H. Knözinger, F. Schüth, J. Weitkamp (Eds.), *Handbook of Heterogeneous Catalysis*, 2nd edn., Wiley, Weinheim, 2008, pp. 100–119.

[84] H.K. Kuo, P. Ganesan, R.J. De Angelis, The sintering of a silica-supported nickel catalyst, *J. Catal.* 64 (1980) 303–319, [https://doi.org/10.1016/0021-9517\(80\)90505-9](https://doi.org/10.1016/0021-9517(80)90505-9).

[85] C.H. Bartholomew, Sintering kinetics of supported metals: new perspectives from a unifying GPLE treatment, *Appl. Catal.* 107 (1993) 1–57, [https://doi.org/10.1016/0926-860X\(93\)85114-5](https://doi.org/10.1016/0926-860X(93)85114-5).

[86] G.D. Weatherbee, C.H. Bartholomew, Hydrogenation of CO₂ on group VIII metals, *J. Catal.* 68 (1981) 67–76, [https://doi.org/10.1016/0021-9517\(81\)90040-3](https://doi.org/10.1016/0021-9517(81)90040-3).

[87] C.H. Bartholomew, R.J. Farrauto, *Fundamentals of Industrial Catalytic Processes*, 2nd edn., Wiley-AlChE, Hoboken, 2005, pp. 41–45.

[88] F. Cavani, F. Trifirò, A. Vaccari, Hydrotalcite-type anionic clays: preparation, properties and applications, *Catal. Today* 11 (1991) 173–301, [https://doi.org/10.1016/0920-5861\(91\)80068-K](https://doi.org/10.1016/0920-5861(91)80068-K).

[89] C.H. Bartholomew, R.B. Pannell, J.L. Butler, Support and crystallite size effects in CO hydrogenation on nickel, *J. Catal.* 65 (1980) 335–347, [https://doi.org/10.1016/0021-9517\(80\)90311-5](https://doi.org/10.1016/0021-9517(80)90311-5).

[90] M. Che, C.O. Bennett, The influence of particle size on the catalytic properties of supported metals, *Adv. Catal.* 36 (1989) 55–172, [https://doi.org/10.1016/S0360-0564\(08\)60017-6](https://doi.org/10.1016/S0360-0564(08)60017-6).

[91] J.K. Nørskov, T. Bligaard, B. Hvolbæk, F. Abild-Pedersen, I. Chorkendorff, C.H. Christensen, The nature of the active site in heterogeneous metal catalysis, *Chem. Soc. Rev.* 37 (2008) 2163–2171, <https://doi.org/10.1039/B800260F>.

[92] J.L. Ewbank, L. Kovarik, F.Z. Diallo, C. Sievers, Effect of metal-support interactions in Ni/Al₂O₃ catalysts with low metal loading for methane dry reforming, *Appl. Catal. A Gen.* 494 (2015) 57–67, <https://doi.org/10.1016/j.apcata.2015.01.029>.

[93] L. Zank, J. Zieliński, The effect of potassium on Ni/Al₂O₃ catalyst in relation to CO/H₂ reaction, *Appl. Catal. A Gen.* 413 (2012) 132–139, <https://doi.org/10.1016/j.apcata.2011.10.048>.

[94] R. Lamber, G. Schulz-Ekloff, Characterization of microstructures in nickel alumina catalysts by analytical electron microscopy, *Surf. Sci.* 258 (1991) 107–118, [https://doi.org/10.1016/0039-6028\(91\)90906-9](https://doi.org/10.1016/0039-6028(91)90906-9).

[95] J. Zieliński, Morphology of coprecipitated nickel/alumina catalysts with low alumina content, *Appl. Catal. A Gen.* 94 (1993) 107–115, [https://doi.org/10.1016/0926-860X\(93\)85001-6](https://doi.org/10.1016/0926-860X(93)85001-6).

[96] L. Zank, J. Zieliński, Interaction of hydrogen with unsupported and supported nickel, *Langmuir* 22 (2006) 8758–8763, <https://doi.org/10.1021/la0605541>.

[97] D.W. Goodman, R.D. Kelley, T.E. Madey, J.M. White, Measurement of carbide buildup and removal kinetics on Ni(100), *J. Catal.* 64 (1980) 479–481, [https://doi.org/10.1016/0021-9517\(80\)90519-9](https://doi.org/10.1016/0021-9517(80)90519-9).

[98] R.D. Kelly, D.W. Goodman, The chemical physics of solid surfaces and heterogeneous catalysis, *Fundamental Studies of Heterogeneous Catalysis* vol. 4, Elsevier Science Publishers, Amsterdam, 1982.

[99] D.W. Goodman, Model catalytic studies over metal single crystals, *Acc. Chem. Res.* 17 (1984) 194–200, <https://doi.org/10.1021/ar00101a007>.

[100] K. Coulter, X. Xu, D.W. Goodman, Structural and catalytic properties of model supported nickel catalysts, *J. Phys. Chem.* 98 (1994) 1245–1249, <https://doi.org/10.1021/j100055a033>.

[101] S.D. Bischke, D.W. Goodman, J.L. Falconer, Carbon monoxide methanation over nickel/alumina thin-film model catalysts, *Surf. Sci.* 15 (1985) 351–357, [https://doi.org/10.1016/0039-6028\(85\)90651-X](https://doi.org/10.1016/0039-6028(85)90651-X).

[102] C.H. Bartholomew, R.B. Pannell, J.L. Butler, Support and crystallite size effects in CO hydrogenation on nickel, *J. Catal.* 65 (1980) 335–347, [https://doi.org/10.1016/0021-9517\(80\)90311-5](https://doi.org/10.1016/0021-9517(80)90311-5).

[103] M.P. Andersson, F. Abild-Pedersen, I.N. Remediakis, T. Bligaard, G. Jones, J. Engbæk, O. Lytken, S. Horch, J.H. Nielsen, J. Sehested, J.R. Rostrup-Nielsen, J.K. Nørskov, I. Chorkendorff, Structure sensitivity of the methanation reaction: H₂-induced CO dissociation on nickel surfaces, *J. Catal.* 255 (2008) 6–19, <https://doi.org/10.1016/j.jcat.2007.12.016>.

[104] H. Hirano, K. Tanaka, A reason for the structure-insensitive catalytic activity of Ni (100) and Ni(111) surfaces for the methanation reaction of CO, *J. Catal.* 133 (1992) 461–466, [https://doi.org/10.1016/0021-9517\(92\)90253-E](https://doi.org/10.1016/0021-9517(92)90253-E).

[105] C.P. Huang, J.T. Richardson, Alkali promotion of nickel catalysts for carbon monoxide methanation, *J. Catal.* 51 (1987) 1–8, [https://doi.org/10.1016/0021-9517\(78\)90232-4](https://doi.org/10.1016/0021-9517(78)90232-4).

[106] E.C. Kruissink, H.L. Pelta, J.R.H. Ross, L.L. Van Reeu, The effect of sodium on the methanation activity of nickel/alumina coprecipitated catalysts, *Appl. Catal.* 1 (1981) 23–29, [https://doi.org/10.1016/0166-9834\(81\)80015-2](https://doi.org/10.1016/0166-9834(81)80015-2).

[107] P. Schoubey, Methanation of CO on some Ni catalysts, *J. Catal.* 14 (1969) 238–246, [https://doi.org/10.1016/0021-9517\(69\)90431-X](https://doi.org/10.1016/0021-9517(69)90431-X).

[108] A. Díaz, J.A. Odriozola, M. Montes, Influence of alkali additives on activity and toxicity of H₂S and thiophene over a Ni/SiO₂ catalyst, *Appl. Catal. A Gen.* 166 (1998) 163–172, [https://doi.org/10.1016/S0926-860X\(97\)00251-2](https://doi.org/10.1016/S0926-860X(97)00251-2).

[109] B. Lundquist, T. Bligaard, J.K. Nørskov, Understanding heterogeneous catalysis from the fundamentals, 1st edn., in: E. Hasselbrink, B. Lundquist (Eds.), *Handbook of Surface Science*, vol. 3, Elsevier Science Publishers, Amsterdam, 2008p. 273.

[110] J.L. Falconer, A.E. Zagli, Adsorption and methanation of carbon dioxide on a nickel/silica catalyst, *J. Catal.* 62 (1980) 280–285, [https://doi.org/10.1016/0021-9517\(80\)90456-X](https://doi.org/10.1016/0021-9517(80)90456-X).

[111] G.D. Weatherbee, C.H. Bartholomew, Hydrogenation of CO₂ on group VIII metals: II. Kinetics and mechanism of CO₂ hydrogenation on nickel, *J. Catal.* 77 (1982) 460–472, [https://doi.org/10.1016/0021-9517\(82\)90186-5](https://doi.org/10.1016/0021-9517(82)90186-5).

[112] M.P. Kiskinova, *Poisoning and Promotion in Catalysis Based on Surface Science Concepts and Experiments* vol. 70, Elsevier Science Publishers, Amsterdam, 1991.

[113] L.M. Aparicio, Transient isotopic studies and microkinetic modeling of methane reforming over nickel catalysts, *J. Catal.* 165 (1997) 262–274, <https://doi.org/10.1006/jcat.1997.1468>.

[114] J. Gao, Y. Wang, Y. Ping, D. Hu, G. Xu, F. Gu, F. Su, A thermodynamic analysis of methanation reactions of carbon oxides for the production of synthetic natural gas, *RSC Adv.* 2 (2012) 2358–2368, <https://doi.org/10.1039/C2RA00632D>.

[115] G. Eigenberger, Catalytic fixed-bed reactors, in: G. Ertl, H. Knözinger, F. Schüth, J. Weitkamp (Eds.), *Handbook of Heterogeneous Catalysis*, 2nd edn., Wiley, Weinheim, 2008, pp. 2075–2106.

[116] F. Polymosí, A. Erdőhelyi, T. Bánsági, Methanation of CO₂ on supported rhodium catalyst, *J. Catal.* 68 (1981) 371–382, [https://doi.org/10.1016/0021-9517\(81\)90106-8](https://doi.org/10.1016/0021-9517(81)90106-8).

[117] C.H. Bartholomew, Sintering kinetics of supported metals: perspectives from a generalized power law approach, *Stud. Surf. Sci. Catal.* 88 (1994) 1–18, [https://doi.org/10.1016/S0167-2991\(08\)62726-3](https://doi.org/10.1016/S0167-2991(08)62726-3).

[118] J. Lif, I. Odenbrand, M. Skoglundh, Sintering of alumina-supported nickel particles under amination conditions: support effects, *Appl. Catal. A Gen.* 317 (2007) 62–69, <https://doi.org/10.1016/j.apcata.2006.10.003>.

[119] J. Lif, M. Skoglundh, L. Löwendahl, Stabilising alumina-supported nickel particles against sintering in ammonia/hydrogen atmosphere, *Appl. Catal.* 274 (2004) 61–69, <https://doi.org/10.1016/j.apcata.2004.05.022>.

[120] Q. Liu, J. Gao, M. Zhang, H. Li, F. Gu, G. Xu, Z. Zhong, F. Su, Highly active and stable Ni/γ-Al₂O₃ catalysts selectively deposited with CeO₂ for CO methanation, *RSC Adv.* 4 (2014) 16094–16103, <https://doi.org/10.1039/C4RA00746H>.

[121] C.H. Bartholomew, R.B. Pannell, R.W. Fowler, Sintering of alumina-supported nickel and nickel bimetallic methanation catalysts in atmospheres, *J. Catal.* 79 (1983) 34–46, [https://doi.org/10.1016/0021-9517\(83\)90287-7](https://doi.org/10.1016/0021-9517(83)90287-7).

[122] D.L. Trimm, Thermal stability of catalyst supports, in: C.H. Bartholomew, J.B. Butt (Eds.), *Catalyst Deactivation*, vol. 68, Elsevier Science Publishers B. V., Amsterdam, 1991, pp. 29–51, [https://doi.org/10.1016/S0167-2991\(08\)62619-1](https://doi.org/10.1016/S0167-2991(08)62619-1).

[123] G. Busca, The surface of transitional aluminas: a critical review, *Catal. Today* 226 (2014) 2–13, <https://doi.org/10.1016/j.cattod.2013.08.003>.

[124] R.L. Augustine, *Heterogeneous Catalysis for the Synthetic Chemist*, 1st edn., CRC Press, New York, 1995.

[125] P. Euzen, P. Raybaud, X. Krokidis, H. Toulhoat, J.-L. Le Loarer, J.-P. Jolivet, C. Froidefond, Alumina, in: F. Schüth, K.S.W. Sing, J. Weitkamp (Eds.), *Handbook of Porous Solids*, 1st edn., Wiley, Weinheim, 2002, p. 1626.